American Mineralogist, Volume 84, pages 1793–1818, 1999

Topology of syntectonic melt-flow networks in the deep crust: Inferences from three-dimensional images of leucosome geometry in migmatites

MARY ANNE BROWN,[1] MICHAEL BROWN,[1,]* WILLIAM D. CARLSON,[2] AND CAMBRIA DENISON[2]

[1]Laboratory for Crustal Petrology, Department of Geology, University of Maryland, College Park, Maryland 20742, U.S.A.
[2]Department of Geological Sciences, University of Texas at Austin, Austin, Texas 78712, U.S.A.

ABSTRACT

We have determined the three-dimensional form of leucosome in two migmatites produced by syntectonic anatexis of different protoliths: (1) stromatic migmatite derived from pelite, which comprises sheets of leucosome (quartzofeldspathic layers with Grt) with walls of melanosome (Bt-rich selvages) in mesosome (schistose layers of Bt + Pl + Qtz ± Grt ± Crd) and (2) a migmatitic garnet-amphibolite derived from basalt, which is composed of spindle-shaped leucosomes (Qtz + Pl), spatially associated with peritectic Grt, in melanosome (Hbl + Qtz ± Cpx). Three-dimensional images were generated from two-dimensional representations of spatial data obtained by two methods: (1) serial grinding and (2) high-resolution X-ray computed tomography (HR X-ray CT). Projections of three-dimensional images of stromatic migmatite derived using data from either method show the planar nature of leucosome throughout the sample; melt transport through this rock when it was partially molten could be modeled as flow in parallel conduits. In the image derived from HR X-ray CT data, garnet in leucosome is only rarely in contact with melanosome, which suggests these garnet grains were suspended in melt during flow. Projections of three-dimensional images of the migmatitic garnet-amphibolite do not reveal the full extent of leucosome connectivity, due to the irregular geometry of leucosome. Connectivity in this sample can be shown, however, by virtual slicing of the three-dimensional images perpendicular to the plane of the two-dimensional representations (approximately parallel to the lineation defined by the leucosome), and by using three-dimensional projections of a single leucosome connectivity "tree" constructed by projecting leucosome patches from slice to slice and noting the overlap. Based on leucosome geometry and volume, we estimate effective porosity for flow in this rock to have been 20 vol% at stagnation. Leucosome in the migmatitic garnet-amphibolite occurs in strain shadows around garnet, which are inferred to have been obstacles to flow along linear paths. Blocking of inferred flow channels by garnet contributes to the high degree of path-length tortuosity in this sample (τ = 2–6), which is expressed visually by the complex form of the leucosome in three dimensions. Cross-sectional areas for individual inferred melt flow paths are highly variable (over 2–3 orders of magnitude) and minimum channel radius is changeable (by ~1 order of magnitude), meaning there was large variability along the channels and implying strong local flow divergences. Based on these data, unusually straight and uniform channels would have dominated the mesoscopic melt flux through this rock when it was partially molten.

INTRODUCTION

One of the fundamental geophysical observations made of the Earth is the stratified nature of the continental crust, in which the lower crust comprises denser, more mafic material and the upper crust comprises less dense, more felsic material. This chemically differentiated layered structure is developed and maintained by partial melting at depth and the ascent of magma to shallower crustal levels. In this paper, we are concerned with the movement of melt in the deep crust while it was in a partially molten state. Information to address this issue is potentially available from anatectic migmatites, which are mixed rocks that comprise: (1) leucosome, representing former melt or its cumulate product, in some cases including residual and peritectic melting products; (2) melanosome, representing residual material, possibly including peritectic melting products; and, (3) mesosome, representing the least depleted material that most closely resembles the protolith in chemical composition. Exposed segments of the deep crust typically are migmatitic, which suggests they preserve evidence of the topology of syntectonic melt flow networks.

The differentiation process begins with anatexis of the deep crust and ends with granite plutonism or rhyolite volcanism: these steps have been studied extensively (e.g., the volumes edited by Ashworth and Brown 1990; P.E. Brown and Chappell 1992; Brown et al. 1995a, 1996; Bouchez et al. 1997). Inter-

*E-mail: mbrown@geol.umd.edu

vening steps involve melt segregation in the source region, transport through the partially molten zone, and ascent across the subsolidus crust to an eventual resting place. Our understanding of these steps is limited by the scarcity of data concerning the properties of crustal melts and the movement of magma under conditions appropriate to the deep crust (e.g., Bagdassarov and Dorfman 1998). Consequently, understanding the mechanisms and rates of melt segregation, the types of melt transport paths, and the mechanisms and rates of magma ascent, particularly during contractional orogenesis, remain important goals of petrology (e.g., Brown and Solar 1998b, 1999).

Granite that is stuck in veins, between boudins, along fold axial surfaces, in shear zones, and in channels and pipes records the plumbing that enabled meso-scale pervasive melt flow through the deep crust (e.g., Brown 1994; Obata et al. 1994; Collins and Sawyer 1996; Brown and Rushmer 1997; Brown and Solar 1999). Where migmatite structures have been described quantitatively, the distribution of leucosome is scale-invariant with distinct fractal dimension (e.g., Tanner 1999). However, because these granite-filled structures define a connected network of structurally controlled flow paths, it is unlikely that transport was driven by buoyancy forces alone, but more likely was a response to deformation of a heterogeneous source subjected to applied differential stress (e.g., Sawyer 1994; Brown et al. 1995b; Brown and Rushmer 1997; Rutter 1997; Brown and Solar 1999).

Field observations of granite in migmatites show that these melt flow networks feed larger planar and cylindrical conduits, which suggests that batches of magma move through plastically deforming, partially molten crust by viscous flow (Brown and Solar 1999). In contrast, at temperatures below the wet solidus, magma may be transported in tensile and/or dilatant shear fractures (e.g., Brown and Solar 1998b). The chemical composition of typical crustally derived granites suggests 10–25 vol% melting of the source, which requires a source volume of four to ten times the volume of the pluton. Thus, extensive lateral migration of melt through the anatectic zone to a site of ascent is implied (Brown and Solar 1999).

The three-dimensional surface defined by the wet solidus represents the periodically drained boundary to the partially molten zone. It is the zero porosity limit for percolative melt flow, due to congelation of melt. The wet solidus represents an unstable interface where flow instabilities may develop. Amplification of these flow instabilities may enable ascent of magma by viscous flow (e.g., Paterson and Miller 1998; Brown and Solar 1999). Alternatively, magma may be transported through tensile and dilatant shear fractures, if melt pore pressure increases to a level sufficient to induce melt-enhanced embrittlement in previously plastically deforming rocks (Davidson et al. 1994; Rutter 1997; Brown and Solar 1998b). Magma extraction is probably a cyclic process, in which the escape of batches of magma moderates local melt pore pressure. How this escape is initiated in partially molten rock is understood poorly. It may relate to viscous compaction in the anatectic zone and large variation in melt pore pressure near the zero porosity limit for percolative melt flow, which may enable magma transport into the subsolidus crust by an elastic shock (Connolly and Podladchikov 1998).

For escape of large batches of melt, an internal interconnected melt flow network representing the storage porosity must be linked to the escape conduit. One factor that controls the flux of melt through the interconnected melt-flow network is the permeability of partially molten crustal materials, but this parameter is not well constrained for the dynamic conditions that characterize natural anatexis during orogenesis. Permeability varies during the melting cycle as melt volume fluctuates; it increases markedly above the interconnective threshold, which is the porosity at which a surface-energy controlled, grain-boundary interconnected melt-flow network is established (Von Bargen and Waff 1986; Laporte and Watson 1995; Lupulescu and Watson 1999). Although a large positive volume change accompanies dehydration melting of muscovite-bearing assemblages, the volume change associated with dehydration melting in biotite-bearing assemblages may be negligible, so that 10 vol% or more of melt may be retained in and along grain boundaries during partial-melting of biotite-bearing protoliths (Rushmer 1999). Thus, the development of an interconnected melt flow network at the onset of dehydration melting is likely only in muscovite-bearing protoliths (Rushmer 1999). For a variety of reasons, therefore, melt segregation may be inefficient at low melt fractions and, without deformation to assist flow, melt in the crust may be nearly stagnant below ~10 vol% (e.g., Brown et al. 1995b; Laporte et al. 1997; Rushmer 1999). To further develop models of melt flow in the deep crust, we need to know the nature of the porosity networks in the source rocks, bearing in mind that these networks may change in response to deformation.

LEUCOSOME—MELT RELATIONSHIP

Several issues must be addressed before any results based on studies of migmatites can be used in the quantification of melt flow through the deep crust. To interpret the leucosome geometry as remnant evidence of an active interconnected melt-flow network in the anatectic zone, we must be sure that the leucosome represents part of the melting/crystallizing system in partially molten crust. A primarily anatectic origin for many migmatites is evidenced by their microstructure (e.g., Vernon and Collins 1988; McLellan 1989; Harte et al. 1991; Brown 1998; Sawyer 1999; Vernon 1999), suggested by geochemical data (e.g., Dougan 1979, 1981; Weber et al. 1985; Sawyer and Barnes 1988; Sawyer 1998), permitted by estimates of *P-T* conditions (e.g., Ashworth 1985; Ashworth and Brown 1990; Vielzeuf and Vidal 1990), and indicated by accumulation of quartzofeldspathic material in dilatant sites formed during syn-anatectic deformation of the protolith (e.g., Brown 1994; Sawyer 1994; Brown et al. 1995b; Brown and Rushmer 1997; Snoke et al. 1999; Vernon and Paterson 1999). Leucosome geometry in these migmatites is inferred to record evidence of active melt flow, rather than stagnant melt, if: (1) bulk-rock compositions are consistent with depletion in felsic components, implying that leucosome was not simply a product of in situ segregation during partial melting; and (2) leucosomes preserve textures resulting from the presence of melt, such as mineral "pseudomorphs" of melt as thin films along grain boundaries and/or solid-melt reaction textures (e.g., Powell and Downes 1990; Harte et al. 1991; Ellis and Obata 1992; Schnetger 1994; Nyman

et al. 1995; Brown and Dallmeyer 1996; Hartel and Pattison 1996; Carson et al. 1997; Brown 1998; Sawyer 1999). We acknowledge, however, that textural analysis in migmatites remains an uncertain science in which care must be exercised to distinguish textures related to melting from those produced by subsolidus processes alone (e.g., Dallain et al. 1999). Some migmatites exhibit evidence of melt-enhanced embrittlement (e.g., Davidson et al. 1994) and leucosomes commonly show microstructures that suggest flow in the magmatic state (e.g., Blumenfeld and Bouchez 1988; Sawyer 1996; Brown and Solar 1998a, 1998b).

Leucosome modes and/or chemical compositions commonly are interpreted to reflect dominance of cumulate and/or residual solid phases after melt escape, rather than melt compositions (e.g., Powell and Downes 1990; Ellis and Obata 1992; Carson et al. 1997). This is problematic for several reasons. During active flow, the inclusion of solid material in the melt may affect the viscosity of the resultant magma, depending upon the relative proportions of solid and melt (Bagdassarov and Dorfman 1998). Furthermore, because viscosity of the magma is an important control on magma flow rate, the effect of entrained solids becomes important as magma flow rate wanes and the proportion of solid to melt increases (Vigneresse et al. 1997; Petford and Koenders 1998). With decreasing flow rate and/or increasing proportion of solid, transport will follow one of two mechanisms: (1) flow of melt around solid particles, particularly if these are pinned in the melt-flow channels; or (2) melt-assisted granular flow (i.e., bulk flow; Rutter 1997)—similar to "suspension flow" as used in the igneous petrology literature for inequant crystals such as feldspar in residual melt (e.g., Nicolas and Ildefonse 1996). We address the issue of flow around solids in the migmatites used in this study, but the question of bulk flow is not addressed here (see Means and Park 1994; Nicolas and Ildefonse 1996; Rutter 1997).

For the leucosome geometry in a migmatite to be a useful proxy for the syntectonic melt-flow network, it must reflect the volume (porosity), topology, and connectivity of that network; however, this may not be the case for several reasons. Multiple melt production/extraction cycles may be represented by leucosome in any migmatite. During anatexis, a rock may undergo cyclic melt-enhanced embrittlement and melt escape. Magma-filled channels of different generations may or may not be interconnected during a particular episode of melt flow. By working at the meso-scale, represented by hand specimens of migmatite in which leucosome is related to one metamorphic cycle, we assume that the risk of analyzing some combination of melt flow networks of different generations is reduced. If melt has leaked from the system during crystallization, the melt flow network may have had a larger volume (porosity) and higher permeability during active flow, in comparison with that implied by the preserved leucosome volume and derived permeability. Although angular relations among leucosomes may change during melt escape and shear-enhanced compaction, the principal effect of melt escape is likely to be the reduction of channel aperture. For these reasons, we interpret the melt-flow network inferred from the leucosome geometry to represent only a minimum estimate of the porosity and connectivity of the meso-scale active melt-flow network.

POROUS MEDIA

Porosity (ϕ) is the pore volume per unit rock volume, which is usually taken to be equivalent to the melt fraction in a partially molten rock. Permeability, which has the dimensions of area, is a measure of the conductivity of the porous medium to fluid flow through it. Although permeability is related to the geometry of the pore system, and not to the properties of the fluid in the pores, the relationship between porosity and permeability is not fixed. For any given material the relationship depends on many factors, including pore sizes, and their geometry, distribution, and connectivity. The porosity does not give any information concerning these factors, so that a partially molten protolith may have low porosity, but if the pores are large and freely connected, the permeability may be high. Thus, partially molten rocks of different protolith composition can have a similar melt fraction, representing the porosity, but different transport properties, such as permeability. Nevertheless, for similar partially molten protoliths with similar melt-flow network structures, it is reasonable to expect that higher porosity (i.e., higher vol% melt) will translate to higher permeability.

Permeability is a transport property that relates the fluid flux to the driving force—the fluid pressure gradient. For slow, steady, unidirectional laminar (Poiseuille) flow of melt through a non-deforming zone, the volume of melt per unit time across a section of porous medium perpendicular to the direction of flow, the flux, q, is linearly proportional to the pressure gradient parallel to the direction of flow, $\mathrm{d}P/\mathrm{d}x$. If the viscosity of the melt is μ,

$$q = \frac{k}{\mu}\frac{\mathrm{d}P}{\mathrm{d}x} \quad (1)$$

where the scaling factor, k, is the intrinsic permeability of the solid medium. This is Darcy's law where the elevation head term is held to be negligible compared with the pressure head term. The flux is not the actual velocity of the fluid in the pores, which is $q^* = q/\phi$. As the porosity is probably in the range ~10–25 vol% in common crustal rocks undergoing anatexis under granulite facies conditions (where porosity is equivalent to melt volume at conditions of 800 ± 50 °C in the deep crust: Clemens et al. 1997; Barboza and Bergantz 1998; Spear et al. 1999), the average velocity of the fluid in the pores probably is between four and ten times larger than the flux. Thus, for a given pressure gradient, the melt flux is essentially controlled by the permeability of the matrix (the porous medium) and the viscosity of the melt. We will not discuss viscosity further, and the reader is referred to the recent literature (e.g., Baker 1996; Clemens et al. 1997; Scaillet et al. 1997; Bagdassarov and Dorfman 1998). This paper is concerned primarily with factors that influence the permeability.

PERMEABILITY IN MIGMATITES

Following pioneering experiments to study initial melting at grain boundaries in natural plutonic rocks and the resulting disequilibrium melt textures (Mehnert et al. 1973; Büsch et al. 1974), exhaustive experimental studies in simple mineral-melt systems involving equilibrium melt textures under applied hydrostatic stress conditions have shown that silicic melt will form

an interconnected grain-boundary network in common crustal protoliths (e.g., Holness 1997; Laporte et al. 1997). Rock-forming minerals, particularly ferromagnesian minerals and feldspars, show some degree of anisotropy of surface energies, which leads to the development of planar, rational, low-energy faces in contact with the fluid (Wolf and Wylie 1991; Laporte and Watson 1995). Thus, under applied hydrostatic stress conditions, the geometry of melt-filled pores may be controlled by the kinetics of reaction and growth of the ferromagnesian minerals and the feldspars, and the interconnected melt-flow network will comprise grain-edged tubes and planar pores along crystal faces (Brown and Rushmer 1997). Although we assume that active deformation will not change the basic geometry of the interconnected melt-flow network at the grain scale, we recognize that this depends on the rate of textural equilibration versus the strain rate. Active deformation should change the rate of melt flow relative to the matrix, however, because the compactional or dilational part of the deformation of the matrix should impart momentum to the melt in the pores. The results of these experimental studies should be relevant to segregation of melt into discrete macroscopic pockets and layers, assuming strain rate is low enough that diffusive mass transfer can maintain an approach to textural equilibrium, which may be important in the early stages of melt segregation. Once the increasing volume of melt leads to a reduction in strength and an increase in strain rate, textural equilibrium is unlikely to be maintained.

For non-texturally equilibrated materials, the permeability cannot be derived analytically (Holness 1997). For such materials, the standard approach is to develop models that relate permeability to features of the pore geometry and the porosity network, and to compare results from these models with experimental determinations of transport properties. To place in context the work we report here on natural samples, we briefly review permeability models (see Appendix 1), which are of two kinds. In network models of partially molten materials, the permeability is described using different pore shapes with different pressure sensitivities to mimic the pore structure arising from the interconnected melt in a crystalline matrix (the porous medium), and the model is an approximation to the real system (e.g., Guéguen and Dienes 1989; Bernabé 1991, 1995). Equivalent porous-medium models use the idea of a hydraulic radius (e.g., Walsh and Brace 1984), in which the pore structure is represented by tubular conduits of different radii. Though topologically unrealistic, these are easily visualized models that capture many features of pore-space structure in partially molten materials. The fundamental difference between these two groups of models is the multiply connected nature of pore space in the network models. Using permeability models such as these is one method to investigate melt flow in the transition from grain-scale segregation of melt in discrete pockets to meso-scale flow of magma in planar- and pipe-like conduits.

In basic geometric models, such as flow in parallel-sided cracks or cylindrical tubes, simple relationships between permeability and porosity can be derived, e.g., $k \propto \phi^3$ and $k \propto \phi^2$ respectively (e.g., Guéguen and Palciauskas 1994). The problem with such geometric simplifications is that most of the macroscopic physical properties of crustal materials are influenced by the pore microstructure, a factor that is not readily incorporated into these models. The pore microstructure is the result of diagenetic processes during burial of sedimentary rocks, syntectonic solid-state processes that involve devolatilization reactions in metamorphic rocks, and syntectonic melting-crystallization processes during progressive fusion of anatectic rocks. Assuming connected porosity, characteristics of the pore microstructure, such as pore-volume surface area (which affects the drag force), path-length tortuosity (a measure of the effective flow-path length taken by a fluid particle through a porous medium), variation in mean pore radius and minimum channel cross-section (which cause local flow divergence and imply significant lineation-parallel nonuniformities), and pore-surface roughness (which reduces the overall efficiency of the flow channels), strongly affect the permeability of sedimentary rocks (e.g., Carman 1937; Thompson et al. 1987; Diedericks and Du Plessis 1995; Aharonov et al. 1997; Clennell 1997). These characteristics are likely to affect fluid flow in the metamorphic realm and melt flow in the anatectic zone similarly, although magma viscosity and the zero porosity limit for percolative melt flow—the solidus—are also important in controlling the rate of magma flow through, and mechanisms of magma escape from, the anatectic zone. Finally, the permeability of crustal materials typically is anisotropic, and we expect that the permeability would be greater parallel to the tectonite fabric than across it, particularly if flow is deformation-assisted and governed by strain partitioning, as suggested by field observations in orogenic belts (e.g., Brown and Solar 1998a, 1998b, 1999).

Attempts to infer the geometry of melt-filled pores from textural studies of crystallized melt-bearing rocks have been inhibited because microstructures are altered during final solidification and subsolidus modification (e.g., Hunter 1987; Harte et al. 1991; Means and Park 1994; Bryon et al. 1996; Nicolas and Ildefonse 1996). We can reduce these problems by regarding the topology of the melt flow network in equigranular, isotropic crystalline protoliths as analogous to pore-space geometry in a sedimentary rock (e.g., Thompson et al. 1987). Consider such a protolith that melts to leave a residue of predominantly quartz, feldspar, and garnet. At moderate melt fraction, the variation of permeability with melt fraction may be approximated by a simple power-law permeability-porosity relationship (e.g., Laporte 1994). At low melt fractions, however, the behavior is more complex. This is because of an accelerated reduction in permeability, which no longer can be expressed as a simple function of porosity, becomes increasingly sensitive to pore geometry, tortuosity, and variation in channel cross-section.

This approach does not consider two important factors: dynamic permeability, and the heterogeneous nature of the crust. During orogenesis, melt migration in the anatectic zone occurs at low-to-moderate melt fractions through texturally evolving rocks with dynamic permeability, which is a consequence of the syntectonic and progressive nature of the partial fusion process. The dynamic permeability characteristic of the anatectic zone is a result of coupling between deformation and melt flow. In partially molten crust that is deforming inhomogeneously, the effective stress generally changes from one point to an-

other (Ord and Henley 1997). During plastic deformation, changes in volume are associated with changes in pore pressure, which cause changes in the effective stress that lead to further plastic deformation and volume change. The changes in pore pressure associated with this process contribute to the pressure gradients that drive melt flow according to Darcy's Law (Ord and Henley 1997). In this way, a feedback relation couples deformation and melt flow. Additionally, during deformation, the heterogeneity of crustal materials is likely to result in the formation of highly conductive flow paths, in which the critical parameter that controls permeability is not average porosity but the geometry of the network of highly conductive flow paths.

In summary, theoretical permeability models based on simplified pore geometry (see Appendix 1) may not be a good representation of percolative melt flow through the anatectic zone during syn-anatectic deformation. To understand melt flow in the anatectic zone, we must determine the geometry of melt-flow networks in different crustal protoliths (e.g., pelite and amphibolite) and characterize their pore microstructure. Approaches that combine three-dimensional images of natural leucosome geometries, as proxies for pore structure distribution, with numerical modelling, particularly using cellular automata, in which global fluid-flow behavior is governed by local interaction rules (Kostek et al. 1992; van Genabeek and Rothman 1996), may yield a more realistic picture of the nature of melt segregation and migration in partially molten crustal protoliths (e.g., Miller 1997). One difficulty with such an approach is the distinction between grain-boundary melt and the porous medium, although careful textural analysis of migmatite leucosomes suggests that residual melt commonly has been "pseudomorphed" by monomineralic films along grain boundaries, so that this distinction should be possible in some cases (e.g., Harte et al. 1991; Sawyer 1999). Our approach should enable us to derive the mesoscopic permeability, although this may greatly underestimate the mean permeability of the larger-scale interconnected melt-flow network in the deep crust. However, since melt must permeate through the mesoscopic permeability to segregate into larger conduits, transport properties derived from studies at the meso-scale are necessary to constrain the evolution of magma extraction from the crust.

Leucosome geometry of natural migmatites

As a first step, we report three-dimensional images of two structurally different migmatites, a stromatic migmatite from the migmatitic core of the southern Brittany metamorphic belt (Fig. 1a, Brown 1983; Jones and Brown 1990), and a migmatitic garnet-amphibolite from the Striding-Athabasca mylonite zone, northern Saskatchewan (Fig. 1b, Williams et al. 1995).

Sample description

The stromatic migmatite is a pelitic rock that comprises sheets of leucosome (quartzofeldspathic layers with Grt) with walls of melanosome (biotite-rich selvages flanking the leucosomes) in mesosome (schistose layers composed of Bt + Pl + Qtz ± Crd ± Grt and accessory minerals). It is an S > L tectonite, reflecting flattening deformation. Peak metamorphic conditions were ~850 °C and ~800–1000 MPa (Brown and Dallmeyer 1996). The migmatitic garnet-amphibolite, which was derived from a basaltic protolith, comprises spindle-shaped pockets of leucosome (primarily Qtz + Pl), spatially associated with peritectic garnet, in melanosome (Hbl + Qtz ± Cpx). It is an L > S tectonite, reflecting constrictional deformation. Peak metamorphic conditions were ~800 °C and ~1000 MPa (Williams et al. 1995).

Jones and Brown (1990) and Williams et al. (1995) presented evidence that the leucosomes in the samples used in this study are products of partial melting reactions. Peak *P-T* conditions are consistent with melt-producing reactions for both rock types, melt flow is suggested by leucosome in syn-deformational dilatant sites, and textural evidence exists for solidification of leucosomes from a melt. In the stromatic migmatite, microstructures that suggest the presence of melt during leucosome crystallization include optically continuous, interstitial quartz (interstitial-xenomorphic texture) between plagioclase crystals, some of which show well-developed euhedral crystal faces, and quartz films along plagioclase-plagioclase grain boundaries interpreted to represent former melt (Figs. 1c and 1d). Williams et al. (1995) interpreted the microstructure in the leucosomes in the migmatitic garnet-amphibolite principally as reflecting subsolidus plastic deformation. In the sample of migmatitic garnet-amphibolite used in this study, however, the primary evidence for subsolidus plastic deformation is undulose extinction in quartz found in leucosome spatially associated with garnet in strain shadows. Plagioclase exhibits compositional zoning and twinning, and does not show preferred crystallographic orientation, although plagioclase and quartz show dimensional orientation parallel to the lineation (Fig. 1e). We interpret these features of the microstructure to be consistent with syntectonic magmatic crystallization and weak subsolidus strain. Subsolidus modification of the microstructure in leucosomes increases away from the strain shadows around garnet. The effects of possible post-crystallization deformation will be addressed in the discussion below.

Three-dimensional images from two-dimensional representations of spatial data

To image geological materials in three dimensions, we may use either destructive or non-destructive methods. One destructive approach is to collect spatial data concerning characteristics of a sample from surfaces of a sequence of parallel slices through the sample, using various imaging methods. Reassembling two-dimensional representations of these spatial data by computer using appropriate protocols yields a three-dimensional image of the microstructure of the sample (Marschallinger 1998a). These destructive methods have been used to understand better the pore structure of sandstone (e.g., Ohashi 1992; Cooper and Hunter 1995), the textural development of granite (Bryon et al. 1995), the pore structure associated with magma mingling in a microdiorite enclave (Petford et al. 1996; Pugliese and Petford 1997), the form of monomineralic plagioclase chains in partially melted basalt (Philpotts et al. 1998), and the three-dimensional patterns of porphyroblast growth and microstructure development in metamorphic rocks (e.g., Johnson 1993; Marschallinger et al. 1993; Johnson and Moore 1996; Daniel and Spear 1998; Marschallinger 1998b, 1998c). The

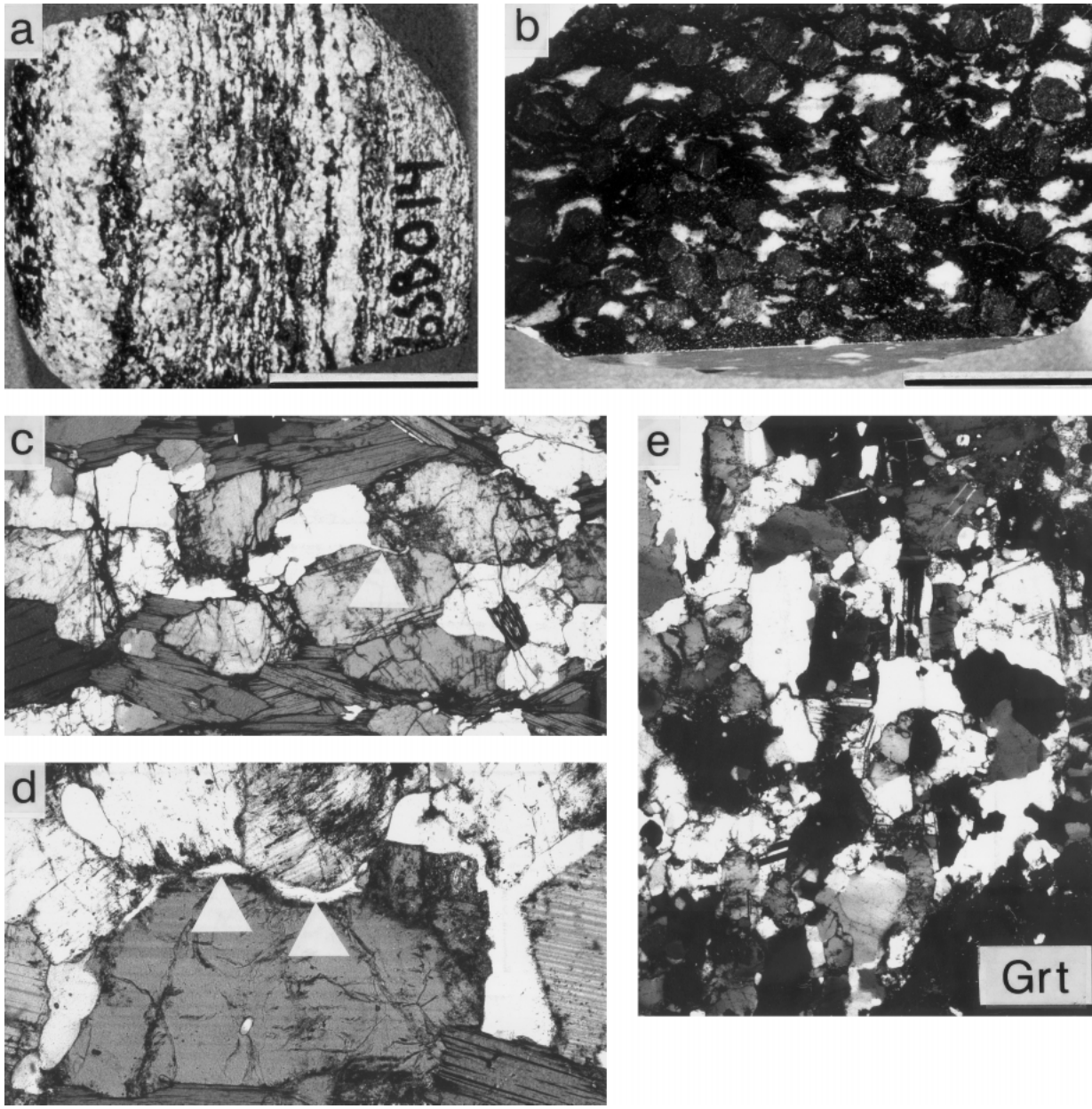

FIGURE 1. (**a**) Cobble of stromatic migmatite from southern Brittany, France (scale bar is 40 mm). (**b**) Block of migmatitic garnet-amphibolite from the Striding-Athabasca mylonite zone, northern Saskatchewan, Canada (scale bar is 50 mm). (**c**) Photomicrograph of blocky plagioclase and interstitial quartz, which locally extends along plagioclase-plagioclase grain boundaries (white arrowhead), in stromatic migmatite (length of photomicrograph is 5 mm). (**d**) Interstitial-xenomorphic texture of quartz around euhedral plagioclase and quartz along plagioclase-plagioclase grain boundaries (white arrowheads) in stromatic migmatite (length of photomicrograph is 2 mm). (**e**) Weak dimensional preferred orientation of quartz and zoned plagioclase crystals (plagioclase shows polysynthetic twinning) parallel to the lineation defined by strain shadows around garnet in migmatitic garnet-amphibolite (length of photomicrograph is 5 mm, Grt is garnet).

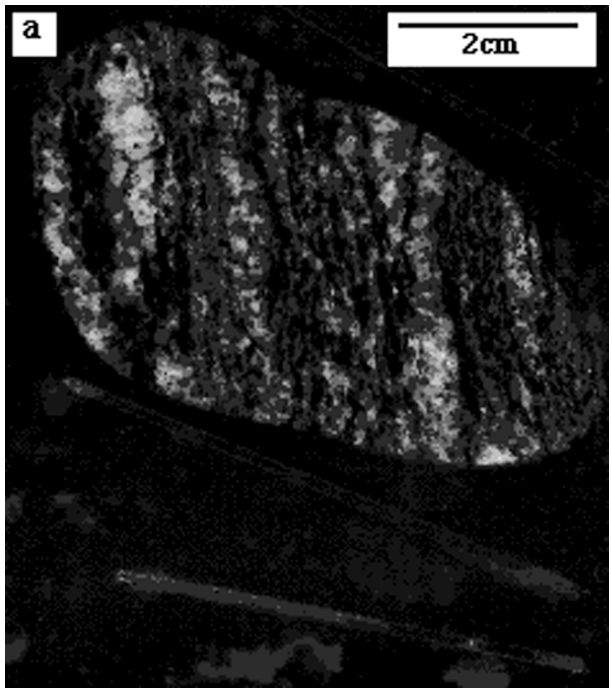

FIGURE 2. (**a**) Cropped, low-resolution, gray-scale representation of the stromatic migmatite. The representation was created by optical scanning of the first slice of a serially ground block of epoxy in which the sample was embedded (upper center of field of view). The white linear features in the epoxy (lower center of field of view) are triangular glass slides used to measure slice thickness. The full-size, higher-resolution, color representation can be found at URLs http://www.minsocam.org and http://www.geol.umd.edu/~maryanne/AM/manuscript.html. (**b**) Animated gif of contrast-enhanced gray-scale representations of 39 serially ground slices of the stromatic migmatite, at URLs http:www.minsocam.org and http://www.geol.umd.edu/~maryanne/AM/manuscript.html. First and last slices are outlined in white. Animation cycles from first to last slice.

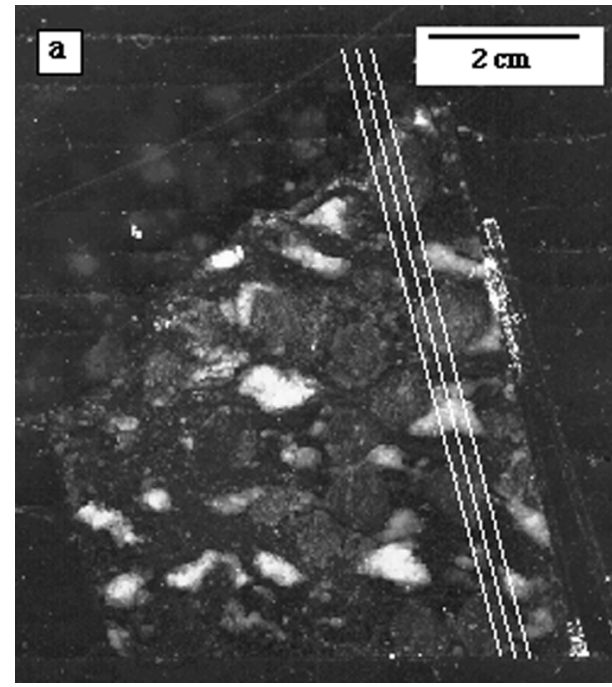

FIGURE 3. (**a**) Cropped, low-resolution, gray-scale representation of the migmatitic garnet-amphibolite. The representation was created by optical scanning of the first slice of a serially ground block of epoxy in which the sample was embedded (center of field of view). The white linear features in the epoxy (right of field of view) are triangular glass slides used to measure slice thickness. The three evenly spaced white lines that cross the scan are reference lines for the cross-sections depicted in Figure 11. The full-size, higher-resolution, color representation can be found at URLs http://www.minsocam.org and http://www.geol.umd.edu/~maryanne/AM/manuscript.html. (**b**) Animated gif of contrast-enhanced gray-scale representations of 42 serially ground slices of the migmatitic garnet-amphibolite, at URLs http://www.minsocam.org and http://www.geol.umd.edu/~maryanne/AM/manuscript.html. First and last slices are outlined in white. Animation cycles from first to last slice.

principal non-destructive method of analysis is high-resolution X-ray computed tomography (HR X-ray CT; e.g., Flannery et al. 1987; Carlson and Denison 1992), which has been applied to determine the geometric structure of pores in sandstone (e.g., Spanne et al. 1994; Auzerais et al. 1996) and to study textures of metamorphic and igneous rocks (e.g., Denison et al. 1997; Denison and Carlson 1997; Bauer et al. 1998; Proussevitch et al. 1998).

Presentation of results. In this paper we display our results as two-dimensional representations of spatial data, sequential displays of stacked two-dimensional representations ("flip-books"), projections of three-dimensional images, and animations of three-dimensional images. These figures are proffered in two groups. The first group of figures is included in the hard copy part of the paper, whereas the second group of figures forms the web-based part of the paper, which may be viewed at URLs http://www.minsocam.org and http://www.geol.umd.edu/~maryanne/AM/manuscript.html.

Methods for obtaining two-dimensional representations of spatial data. Two methods for obtaining two-dimensional spatial data were used. A cobble of stromatic migmatite and half a large sample of the migmatitic garnet-amphibolite specimen were analyzed by the destructive technique of serial grinding. Subsequently, a second cobble of stromatic migmatite and the remaining migmatitic garnet-amphibolite were imaged using the non-destructive technique of high-resolution X-ray computed tomography at the University of Texas, Austin. Because the destructive serial-grinding method was attempted before the non-destructive HR X-ray CT method, the three-dimensional images produced are not of the same volumes of rock, but are from similar samples. The samples were oriented similarly in both methods. For the stromatic migmatite, the serial cuts and the HR X-ray CT scans were oriented perpendicular to the stromatic layering and approximately perpendicular to the mineral elongation lineation. For the migmatitic garnet-amphibolite, the serial cuts and the HR X-ray CT scans are in the plane approxi-

mately perpendicular to the lineation defined by the orientation of hornblende crystals and the spindle-shaped leucosomes.

During serial grinding, each sequential two-dimensional cut (Figs. 2 and 3) was produced by shaving ~1.5 mm off each sample using a rock saw. To enhance contrast, spray varnish was applied to the newly exposed surface before it was photographed and scanned, using a flatbed scanner, to provide a permanent record of each slice. Because the sample had to be removed from the saw carriage after each slice, the samples were embedded in a rectangular block of epoxy to aid in the precise replacement of the block in the carriage. Triangular glass slides were included in the epoxy matrix oriented perpendicular to the grinding plane, so that slice thickness could be calculated. Irregularities in both the block of epoxy and the saw carriage resulted in variations in thickness of slices between ~1 and 2 mm and in the angle of the grinding plane of ±10°. The scans created were 24-bit color TIFF files to maximize image quality. Each scan was associated with its own unique color look-up table. Because the look-up tables were different among the files, standardized image-analysis processes, including comparison of images and compilation of scans into three-dimensional images, were not feasible. Therefore, the scans were converted to gray scale. Image analysis of color scans would have been possible with the use of 8-bit color TIFF files with a standard look-up table.

Two-dimensional representations of spatial data were produced by HR X-ray CT (Figs. 4 and 5), which is an imaging technique that maps the variation of X-ray attenuation within solid objects (Carlson and Denison 1992; Denison et al. 1997). X-ray attenuation depends on mass density and mean atomic number, and the X-ray beam energy; in petrologic applications, each mineral is commonly characterized by a small and distinctive range of attenuation values. In a typical CT scan, a fan-shaped X-ray beam passes through an object, and the transmitted X-ray intensity is measured by an array of collectors, then compared with the intensity of the incident beam to determine the total amount of attenuation. The object is rotated in the X-ray beam, and the resultant attenuation is measured along several paths. Computed tomography calculates the X-ray attenuation at tens of thousands of points in a two-dimensional virtual slice through the object. Each slice is of a fixed thickness, determined principally by the resolution required. Because each measurement is an average over the width of the slice, thinner slices can image smaller objects in the sample and produce sharper edges between objects that have a contact oblique to the plane of the slice. For the stromatic migmatite, we used a 115 mm field of view and produced 108 virtual slices at a spacing of 0.45 mm. For the migmatitic garnet- amphibolite, we used an 80 mm field of view and produced 112 virtual slices at a spacing of 0.45 mm. The two-dimensional representations produced are gray-scale TIFF files of 512×512 pixels.

Comparison between methods. Serial grinding does not require sophisticated instrumentation, as needed for HR X-ray CT, but it is a labor-intensive process, whereas producing each virtual slice for samples similar to those used in this study, after calibration of the machine, takes ~1–4 minutes. In this study, several difficulties were experienced with the optical scans produced in the serial-grinding method. The leucosomes show a range of color from white to rust due to weathering, which created a problem when attempting to identify leucosome by its color. The slight amount of weathering, which was enough to discolor some leucosomes in our samples, was not enough to alter the minerals, so the mass density and mean atomic number of the leucosome minerals did not change with degree of weathering. As a result, we could identify leucosome more consistently in the two-dimensional representations derived from the HR X-ray CT scans.

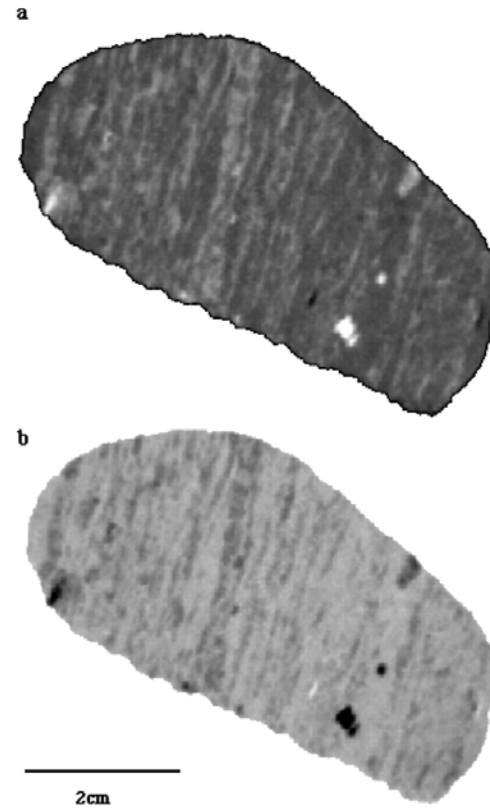

FIGURE 4. (**a**) HR X-ray CT scan of stromatic migmatite. Thickness of scan is 0.45 mm. (**b**) HR X-ray CT scan with gray scale inverted so that leucosome appears light, melanosome appears gray, and garnet appears dark. (**c**) Animated gif of representation of 108 HR X-ray CT scans of the stromatic migmatite in which the gray scale was inverted, at URLs http://www.minsocam.org and http://www.geol.umd.edu/~maryanne/AM/manuscript.html. First and last slices are outlined in white. Animation cycles from first to last slice.

An additional problem in serial grinding using a saw is the removal of a uniform layer to produce slices of constant thickness. This may be problematic for quantitative analysis of the three-dimensional image produced from the two-dimensional representations if variation in the orientation of the surfaces cannot be accommodated. Furthermore, the spacing between the two-dimensional representations limits the quality of the three-dimensional image that can be produced. In serial grinding, the spacing between surfaces is determined by the method of removal of material (saw or large lap), so that the thickness between the two-dimensional images may be greater than (saw) or

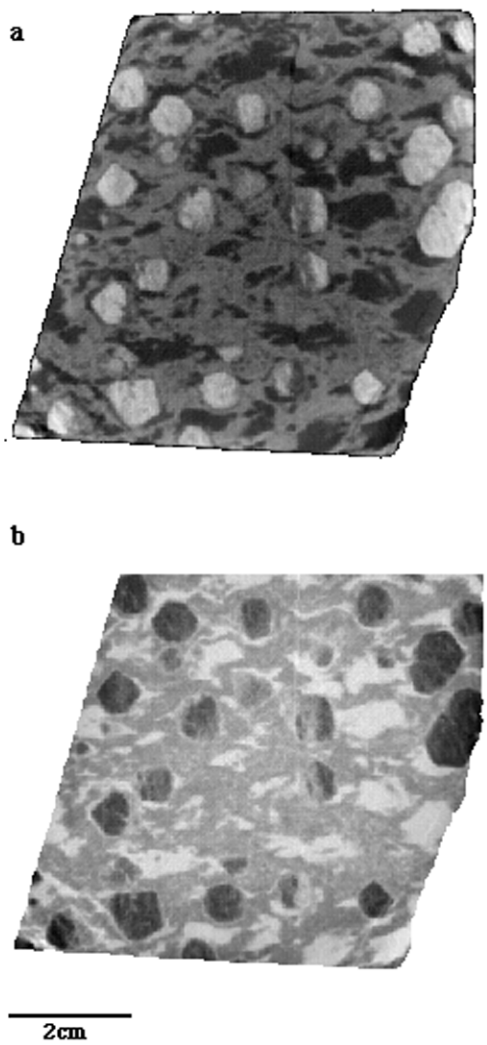

FIGURE 5. (**a**) HR X-ray CT scan of migmatitic garnet-amphibolite. Thickness of scan is 0.45 mm. (**b**) HR X-ray CT scan with gray scale inverted so that leucosome appears light, melanosome appears gray, and garnet appears dark. (**c**) Animated gif of representation of 112 HR X-ray CT scans of the migmatitic garnet-amphibolite in which the gray scale was inverted, at URLs http://www/minsocam.org and http://www.geol.umd.edu/~maryanne/AM/manuscript.html. First and last slices are outlined in white. Animation cycles from first to last slice.

similar to (large lap) those produced by HR X-ray CT. Finally, the number of X-ray scans may be limited by the cost involved, whereas the number of serially ground surfaces is limited only by the time involved.

The main disadvantage of the serial-grinding technique is its destructive nature. Samples imaged with HR X-ray CT can be used later for chemical and isotopic analysis, whereas serially ground samples are lost in the grinding process. Serial grinding does offer one unique advantage, which is the opportunity to examine in detail multiple serial surfaces through the rock sample. Furthermore, a permanent photographic record can be made of each of these rock surfaces. Overall, the best approach is likely to be a combination of each method, with selection of critical areas that can be examined in detail, e.g., by serial grinding or cutting petrographic thin sections, and the location of specific sites of interest for chemical analysis within a sample volume being based on a three-dimensional image produced from two-dimensional representations of spatial data obtained using HR X-ray CT.

Compilation of three-dimensional images from two-dimensional representations of spatial data. Two-dimensional representations of spatial data done at the University of Maryland were analyzed on a Macintosh computer using the public domain NIH Image program developed at the U.S. National Institutes of Health (available on the Internet at http://rsb.info.nih.gov/nih-image/). Three-dimensional images created from the two-dimensional representations of spatial data done at the University of Texas (Figs. 9, 10, 16, and 17) were created using VoxBlast software.

The first step in creating three-dimensional images of leucosome geometry from two-dimensional representations of spatial data is to establish criteria for determining what is to be regarded as leucosome in each two-dimensional representation (thresholding). Gray-scale thresholding was applied to both types of representations using a protocol similar to the p-tile method (Doyle 1962; Sahoo et al. 1988). This method assumes a knowledge of the areal proportion of the objects of interest in a representation, and the threshold between objects and background is the value at which the percentage of pixels below this value matches the known areal percentage for the object. For both types of migmatite, however, the areal percentage of leucosome in the two-dimensional representations is unknown. Therefore, the threshold could not be determined automatically. To place the threshold at the edge of the leucosome, its position was manipulated manually while viewing the image, and its position was adjusted until it was at the edge of the leucosome. This presented a problem in dealing with the two-dimensional representations produced by HR X-ray CT, because they show a "beam-hardening" effect in which the centers of the representations are darker than the edges (Denison et al. 1997). This is due to the polychromatic nature of the X-ray beam used in the scanning process. The lower energies of the imaging X-ray beam spectrum are more strongly absorbed, changing the energy spectrum of the beam during the scan. Using more elaborate scanning techniques than were applied in this pilot study, such beam-hardening artifacts generally can be eliminated. In this study, an empirically determined radial correction factor was applied to the HR X-ray CT representations, so that leucosomes could be isolated using thresholding (Fig. 6).

A three-dimensional image of the leucosome was produced for each sample, using NIH Image for the serial sectioning (Figs. 7 and 8) and VoxBlast for the HR X-ray CT (Figs. 9 and 10). The two-dimensional representations from each sample were assembled into a stack with slice spacing equal to the average slice thickness. A threshold was selected for each stack based on the methods described above, with only slight variation in the threshold values for the individual slices in three of the four stacks. For the stack of images of the serially ground stromatic migmatite, however, it was necessary to change gray-scale levels of some individual slices of that stack to create a more uniform threshold

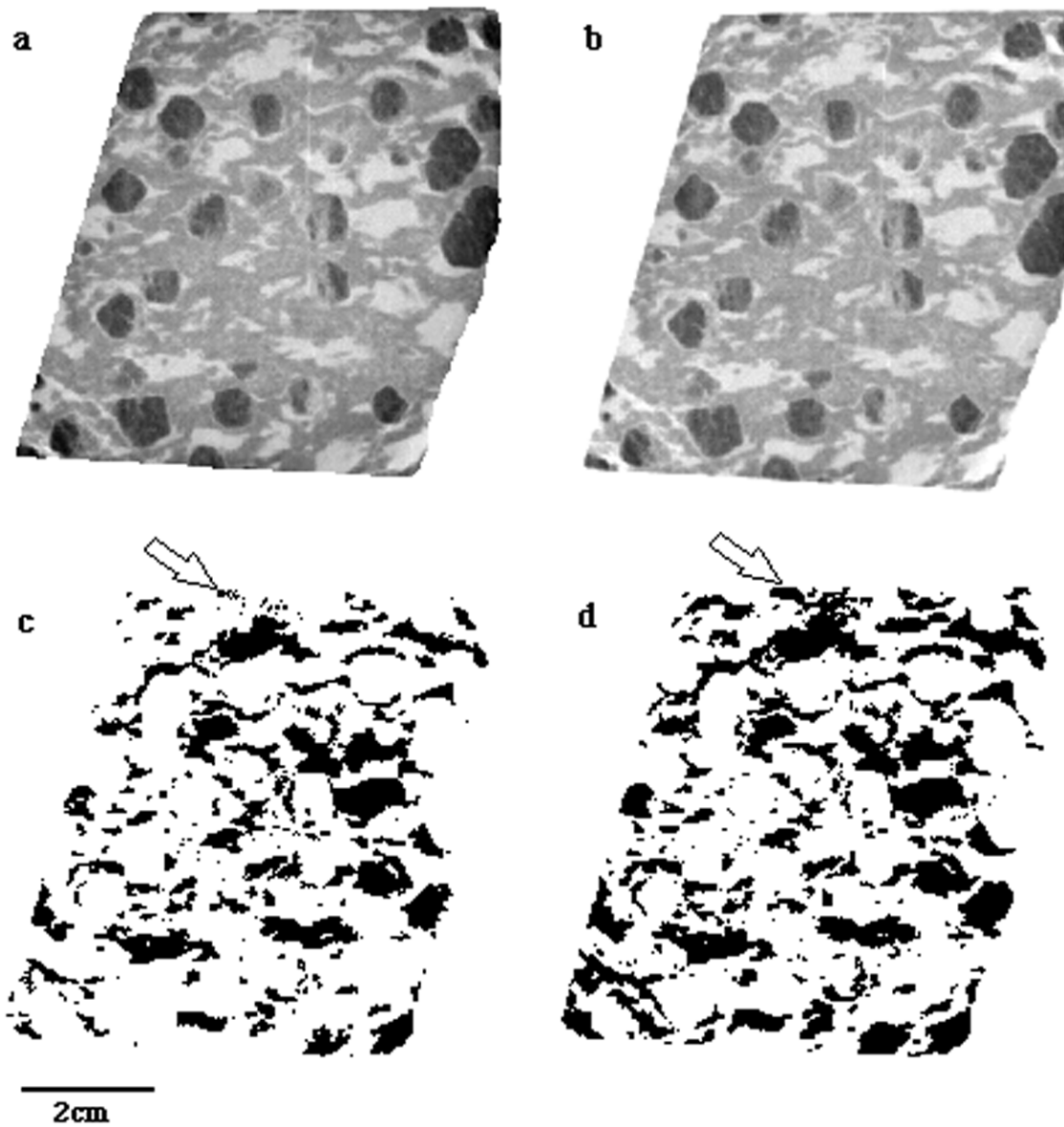

FIGURE 6. (**a**) Representation of HR X-ray CT scan of migmatitic garnet-amphibolite with gray scale inverted. Note that the center of the representation appears lighter than the edges due to beam-hardening. (**b**) HR X-ray CT scan corrected by application of an empirically determined radial correction factor. (**c**) Thresholding applied to the uncorrected scan; arrow shows area where thresholding did not identify leucosome (black). (**d**) Thresholding applied to corrected scan; arrow shows identification of leucosome at edge of scan.

value for the stack (see Fig. 2b for altered images of the stromatic migmatite). All pixel values that were above the threshold value were rendered transparent, and projections were created in which the stack is rotated through 360° around a horizontal axis within the plane of the computer screen. The projections have a "light source" near the eye of the viewer so that objects in the front of the rotating sample are brighter.

The three-dimensional images that result for each sample are different in contrast and amount of detail. These differences reflect the use of NIH image versus VoxBlast (images produced in VoxBlast have greater contrast) and the spacing between the two-dimensional representations (scans produced by HR X-ray CT are more closely spaced and allow interpolation from scan to scan to "complete" the three-dimensional image). The problem of spacing between the two-dimensional representations derived by each method is exacerbated by using NIH image for stacking the representations derived from serial grinding, because, unlike VoxBlast, NIH image does not calculate a virtual volume for the three-dimensional image.

Leucosome geometry in stromatic migmatite

In projections of the three-dimensional images of the stromatic migmatite, several leucosomes traverse each image and present a clear illustration of their planar nature (Figs. 7 and 9).

Leucosome in the stromatic migmatite clearly is connected across the sample. Melt flow through this rock when it was partially molten could be modeled as flow in parallel conduits.

Leucosome geometry in migmatitic garnet-amphibolite

For the migmatitic garnet-amphibolite, leucosome connectivity across the sample is difficult to establish from preliminary inspection of the projections of the three-dimensional images based on the serial-grinding method. To clarify the leucosome connectivity, the stacks of two-dimensional representations of the migmatitic garnet-amphibolite sample were "resliced" perpendicular to the grinding plane, and some of these slices suggest connectivity across the sample (Fig. 11).

Further analysis to determine connectivity, effective porosity for flow, and tortuosity of inferred flow paths was done on the two-dimensional representations of the HR X-ray CT virtual slices through the migmatitic garnet-amphibolite. Effective porosity is the percentage of the pore space that is part of the connected pore system. Therefore, the measure of effective porosity depends upon the extent of connectivity. For migmatite, the leucosome records residual porosity as melt flow waned and the flow network congealed. Thus, the leucosome topology represents a snapshot only, and non-connected leucosome could have been connected previously. Using this measure of effective porosity in reservoir studies is useful because it is linked to the fluid that can be extracted from a rock, but it is less useful when attempting to determine melt flow rates through a rock because it includes dead ends within the connected pore system that do not support flow. The purpose of this study is to define parameters that will constrain melt flow rates through migmatites; therefore, we seek to calculate the effective porosity for flow, i.e., the connected porosity minus the porosity associated with dead ends. Pore roughness can decrease the effective porosity for flow (Aharonov et al. 1997), but flow separation may be a consequence (Middleton 1997); pore roughness was not included in our analysis. Finally, we have determined the path-length tortuosity of 20 through-going channels in the migmatitic garnet-amphibolite.

Effective porosity and tortuosity determinations require the identification and characterization of any through-going channels in the sample. The HR X-ray CT scans of the migmatitic garnet-amphibolite, however, were not perpendicular to the linearity of the leucosomes, assumed to be the direction of greatest connectivity. We determined the direction of the lineation by a three-step process, after leucosome in each image was identified by thresholding as described above. First, best-fit ellipses were created for each leucosome in the first HR X-ray CT scan and the average long dimension determined (Fig. 12). Then the stack of scans was digitally resliced perpendicular to the plane of the original scans, and parallel to the long dimension of leucosomes in the first scan, and the average long dimension of the leucosomes in this slice was determined as above. The direction of this long dimension in space is the lineation direction.

Assuming melt flow was parallel to the lineation, we constructed the geometry of individual melt-flow paths as follows. We compared two adjacent slices; if the area corresponding to leucosome on one image projected onto the next slice and overlapped with leucosome in that slice, the two leucosomes were considered part of a three-dimensional structure that spans two slices. To determine overlap, each leucosome was offset in the direction of the lineation before being compared with the next scan. Connectivity across the entire sample was determined in this way. This method is directional from one side of the sample to the other and, because leucosome structures branch, allows for dead ends to be included in the connected channels. The same procedure was run in the opposite direction on the established channel to eliminate dead ends (Fig. 13). To determine the ratio of effective porosity to total porosity, the area of the eliminated dead ends was compared with the area of the total channel.

Paths that link the centers of leucosomes, identified as the center of the best-fit ellipse with the same area, through the connected channel were constructed and measured. The resultant flow-path length was divided by the distance from the center of the leucosome on the first slice to the center of the leucosome on the last slice to determine the path-length tortuosity. The path-length tortuosity is similar to hydraulic tortuosity as used in the Kozeny-Carman equation (see Appendix 1), rather than geometrical tortuosity (see Appendix 1 and discussion in Clennell 1997).

Ambiguity concerning the connected nature of the leucosome in the migmatitic garnet-amphibolite is due to the complex, irregular shape of the leucosome (Figs. 8 and 10) and its spatial association with garnet (Fig. 5c). By projecting the leucosomes from each slice onto the next and noting their overlap, in the stack of two-dimensional representations derived from the HR X-ray CT, we have determined connectivity across the sample. Tracing the connectivity of a single leucosome from the first HR X-ray CT scan through the stack of scans leads to the discovery of a connectivity tree with several branching structures (Fig. 14). If leucosome in this sample records a fossil melt-flow network, the interconnective threshold was clearly exceeded. By comparing the areal extent of leucosome in each slice with the total slice area, we have determined that leucosome comprises 22% of the migmatitic garnet-amphibolite. In two connectivity trees, leucosome in dead ends was 9% and 11% of the whole leucosome volume, suggesting that a reasonable estimate for the minimum effective porosity for flow (i.e., at stagnation) in the migmatitic garnet-amphibolite was 20 vol%.

A single inferred melt flow path traced through this tree is sinuous (Fig. 15). We have determined path-length tortuosity, τ (see Appendix 1), for twenty measured flow paths, which lie in the range from 2.2 to 5.9 (Table 1). If we examine the effect of τ on the volumetric flux, q, using Equation 1 and an equivalent porous-medium model of permeability, such as the modified Kozeny-Carman Equation A11, a τ of two produces a flux four times slower than through a straight channel, and a τ of six reduces flux rate by a factor of thirty six. This relationship implies that tortuosity, or in broader terms the geometry of the melt-flow network, can affect melt flow rates in the anatectic zone. Besides high tortuosity, individual inferred flow paths have: (1) highly variable cross-sectional areas (by two-to-three orders of magnitude, Table 1), and (2) changeable minimum channel radius (by approximately one order of magnitude, re-

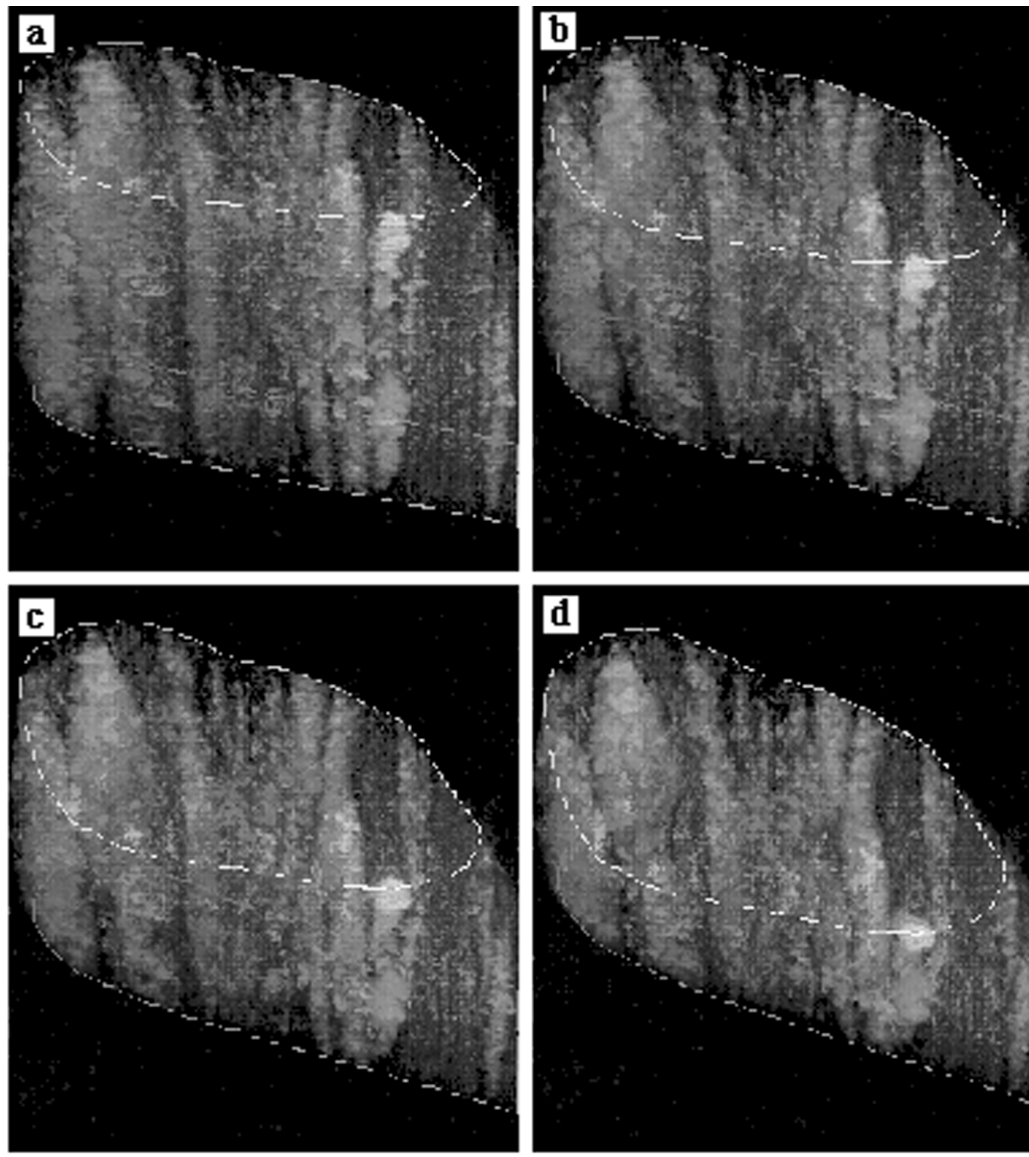

FIGURE 7. Projections of the three-dimensional image of the stromatic migmatite. This image was created using NIH Image to compile into a stack the two-dimensional representations created by scanning after serial grinding. Each slice in the stack can be thought of as a one-pixel-thick plane separated by the thickness of material cut off the sample (~1.5 mm). The stack was rotated around a virtual horizontal axis in the plane of the page through 30° at 10° intervals to produce views **a–d**. A scale bar is not presented because these are projections of a three-dimensional image (Fig. 2a contains the scale for the first image in the stack). The light colored parts of the migmatite (leucosome and felsic minerals in the mesosome) are represented as white and gray. The dark parts of the migmatite (melanosome and mafic minerals in the mesosome) are represented as transparent. Because the melanosome is transparent, these projections present the three-dimensional structure of individual planar leucosomes. (**e**) Animated gif of projection of three-dimensional image rotating through 360°, at URLs http://www.minsocam.org and http://www.geol.umd.edu/~maryanne/AM/manuscript.html.

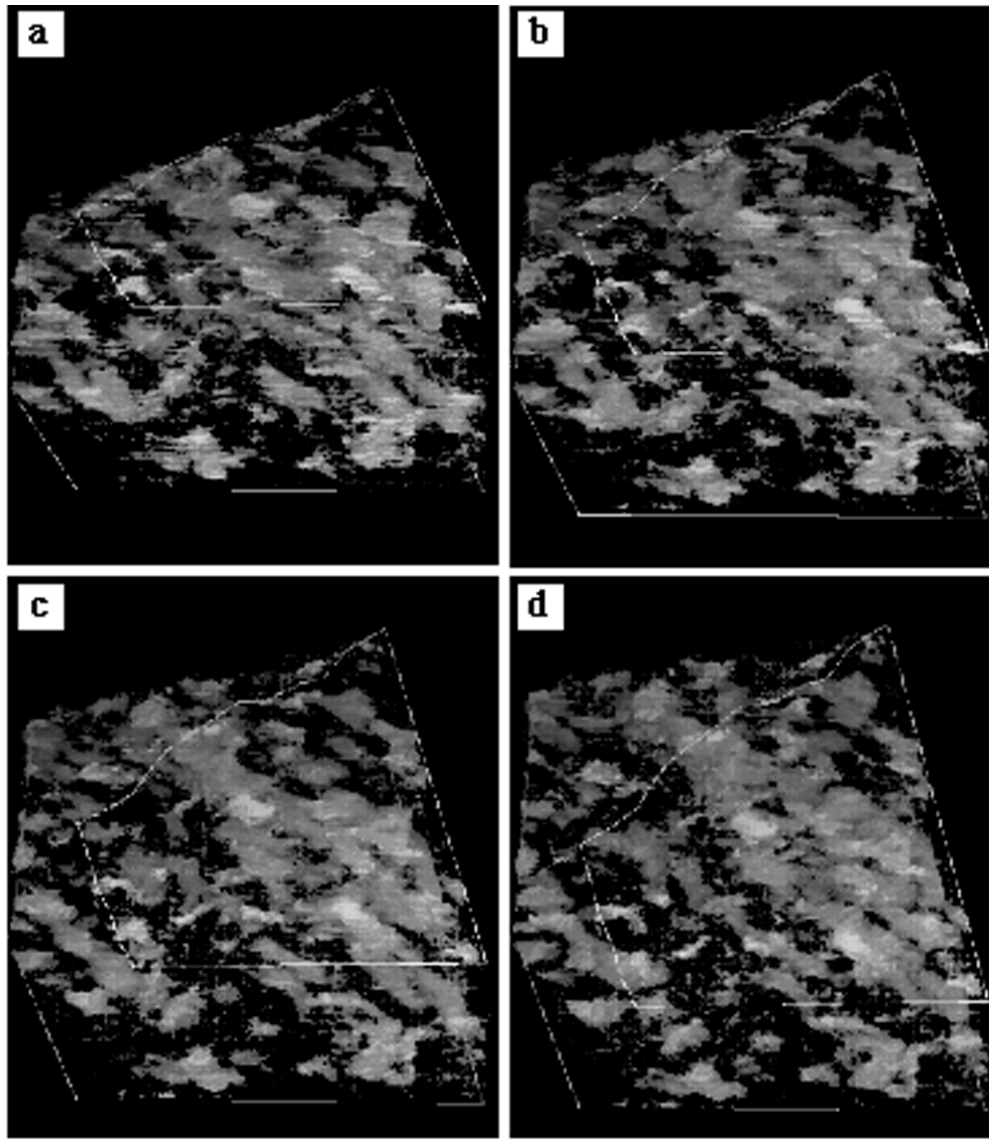

FIGURE 8. Projections of three-dimensional images of the migmatitic garnet-amphibolite. This image was created using NIH Image to compile into a stack the two-dimensional representations created by scanning after serial grinding. Each slice in the stack can be thought of as a one-pixel-thick plane separated by the thickness of material cut off the sample (~1.5 mm). The stack was rotated around a virtual horizontal axis in the plane of the page through 30° at 10° intervals to produce views **a**–**d**. A scale bar is not presented because these are projections of a three-dimensional image (Fig. 3a contains the scale for the first image in the stack). The leucosome and felsic minerals in the mesosome are represented as white and gray. The melanosome and garnets are transparent. Because the leucosome is irregular, it is difficult to perceive the leucosome connectivity in three dimensions. (**e**) Animated gif of projection of three-dimensional image rotating through 360°, at URLs http://www.misocam.org and http://www.geol.umd.edu/~maryanne/AM/manuscript.html.

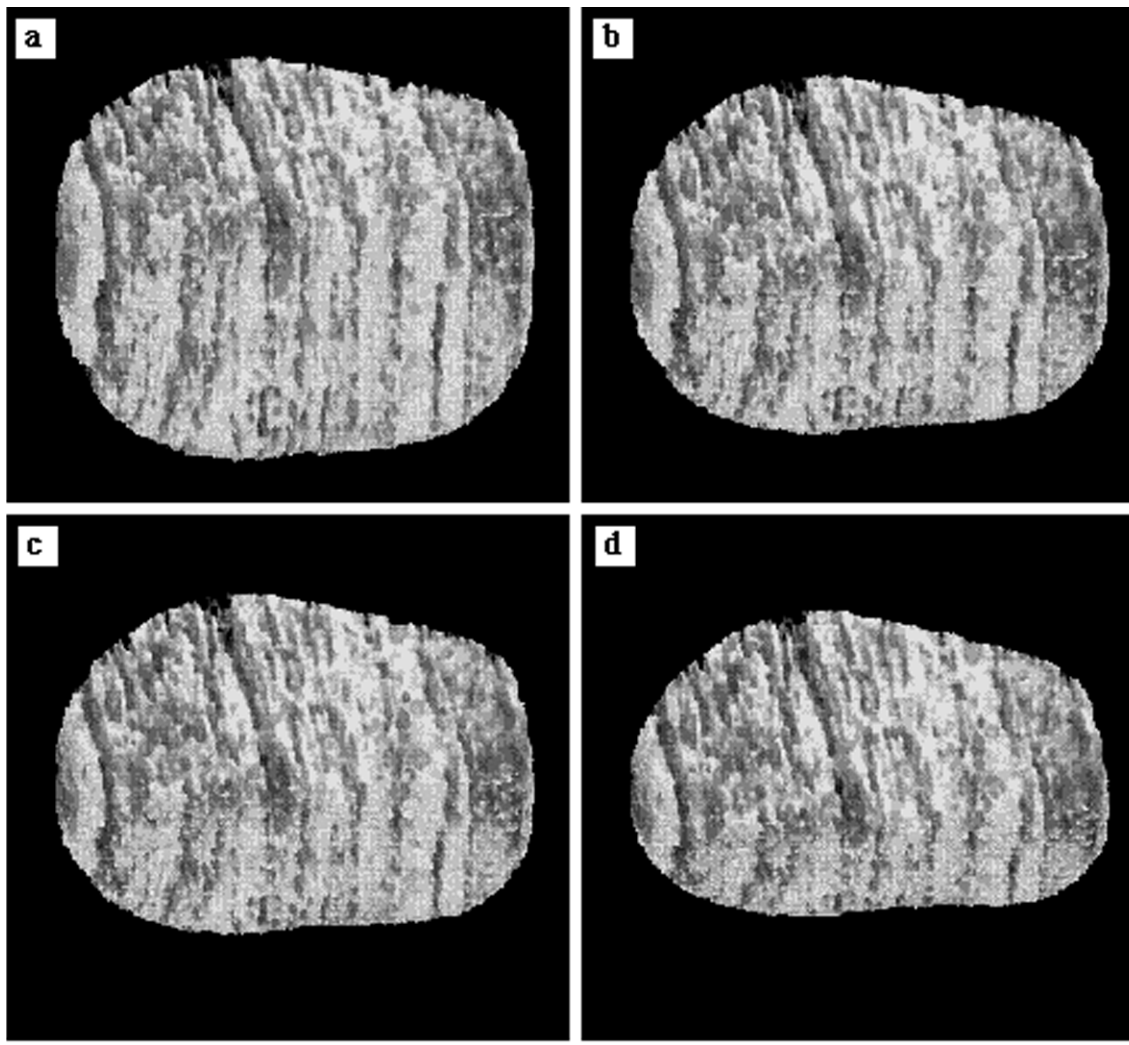

FIGURE 9. Projections of three-dimensional image of the stromatic migmatite. This image was created using VoxBlast to compile into a stack the two-dimensional representations of the HR X-ray CT scans. The three-dimensional image produced is superior to the one created using NIH Image using two-dimensional representations created by scanning after serial grinding (Fig. 7) because the HR X-ray CT scans are more closely spaced and VoxBlast calculates a virtual volume from the stack of two-dimensional representations. The stack was rotated around a virtual horizontal axis in the plane of the page through 30° at 10° intervals to produce views **a**–**d**. A scale bar is not presented because these are three-dimensional projections (Fig. 4b contains the scale for the first image in the stack). The less-dense parts of the migmatite (leucosome and felsic minerals in the mesosome) are represented as white and gray. The denser parts of the migmatite (melanosome and mafic minerals in the mesosome) are transparent. Because the melanosome is transparent, these projections present the three-dimensional structure of individual planar leucosomes. (**e**) Animated gif of projection of three-dimensional image rotating through 360°, at URLs http://www.minsocam.org and http://www.geol.umd.edu/~maryanne/AM/manuscript.html.

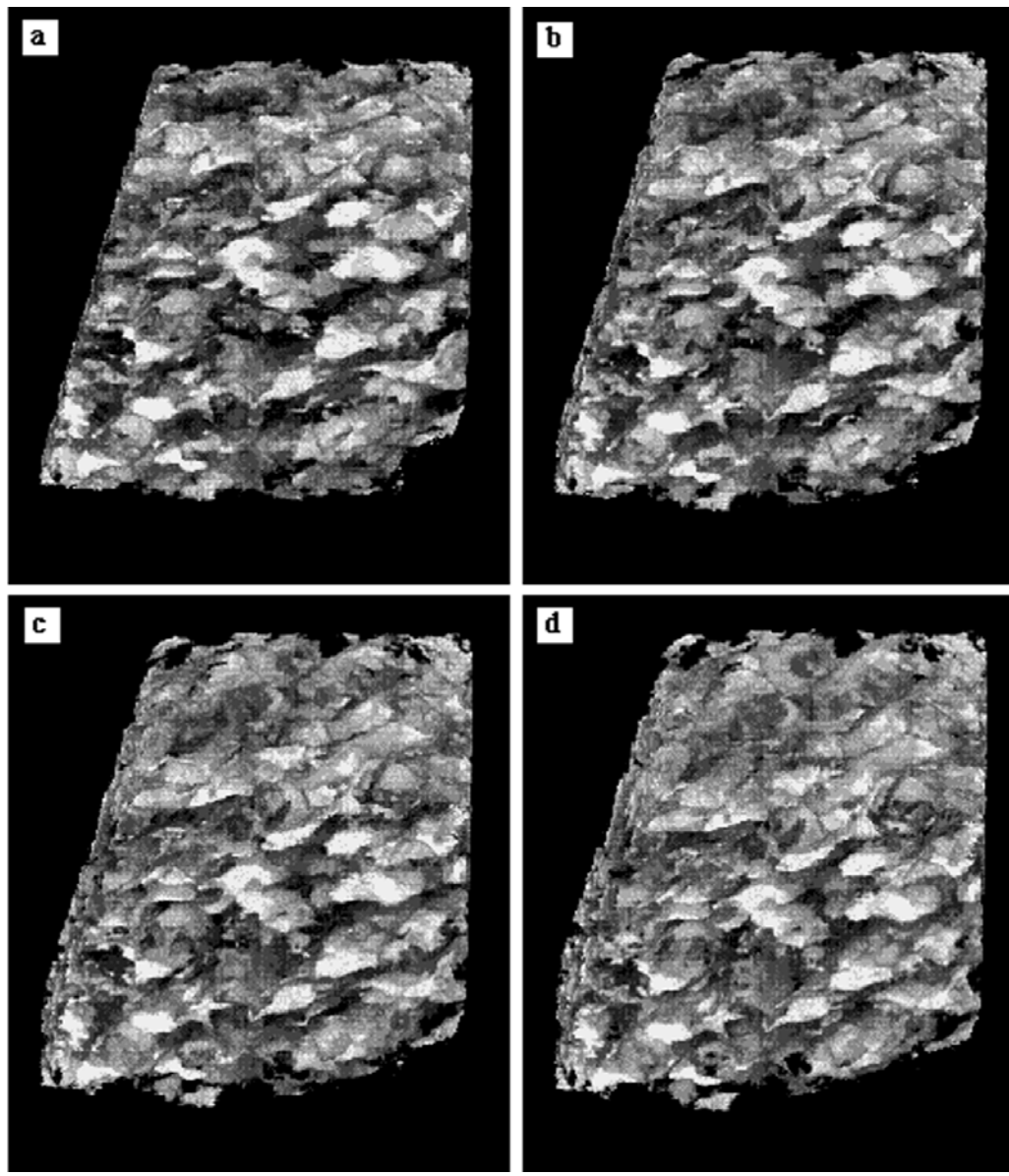

FIGURE 10. Projections of three-dimensional image of the migmatitic garnet-amphibolite. This image was created using VoxBlast to compile into a stack the two-dimensional representations of the HR X-ray CT scans. The three-dimensional image produced is superior to the one created using NIH Image using two-dimensional representations created by scanning after serial grinding (Fig. 7) because the HR X-ray CT scans are more closely spaced and VoxBlast calculates a virtual volume from the stack of two-dimensional representations. The stack was rotated around a virtual horizontal axis in the plane of the page through 30° at 10° intervals to produce views **a**–**d**. A scale bar is not presented because these are projections of a three-dimensional image (Fig. 5b contains the scale for the first image in the stack). The leucosome and felsic minerals in the melanosome are represented as white and gray. The melanosome and garnets are transparent. Because the leucosome is irregular, it is difficult to perceive the leucosome connectivity in three dimensions. (**e**) Animated gif of projection of three-dimensional image rotating through 360°, at URLs http://www.minsocam.org and http://www.geol.umd.edu/~maryanne/AM/manuscript.html.

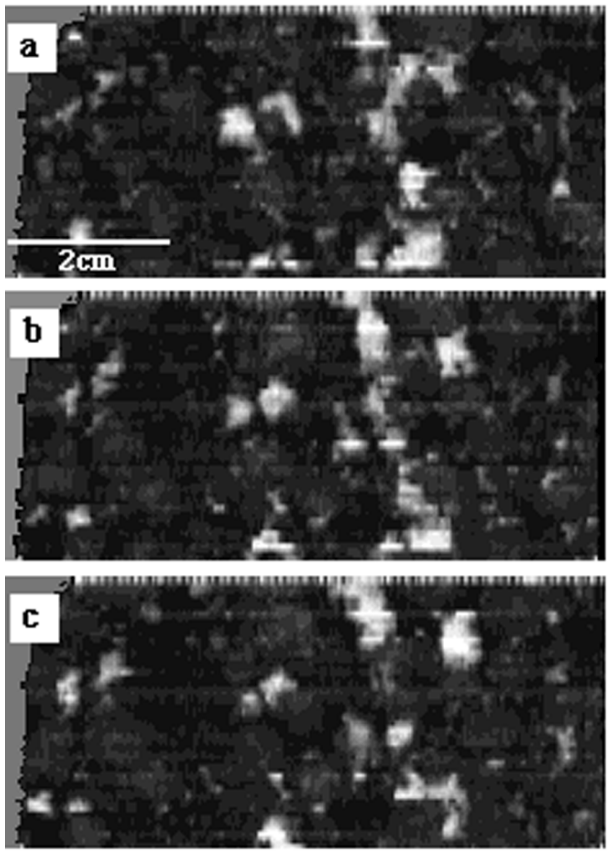

FIGURE 11. Leucosome connectivity of migmatitic garnet-amphibolite shown in computer-generated virtual slices perpendicular to the grinding plane. Each of the original two-dimensional representations of the serially ground surfaces was assigned a thickness in pixels based on slice thickness. These virtual slabs were then compiled into a stack and digitally resliced using NIH Image. (**a**–**c**) The vertical cross-sections in the locations depicted in Figure 3(a) by the right, center, and left white lines. Although the virtual slices through the sample are closely spaced, connectivity only occurs in the center slice. This is to be expected in this migmatitic garnet-amphibolite as the leucosomes are sinuous and do not lie in any single plane.

flected in minimum cross-sectional areas that vary by up to fifty times, Table 1). These features mean there were large variations along the channels, which imply strong local flow divergences. Consequently, we anticipate that unusually straight and uniform channels would dominate the volumetric flux, because the velocity of melt in these channels is larger.

DISCUSSION

Besides the powerful ability of HR X-ray CT to provide a stack of virtual slices that may be used for quantitative analysis in three dimensions, both the two-dimensional representations and the three-dimensional images of leucosome distribution in migmatites are valuable sources of qualitative information. For example, the relationship between garnet and leucosome is distinctly different in the stromatic migmatite (Figs. 4c and 16) and the migmatitic garnet-amphibolite (Figs. 5c and 17).

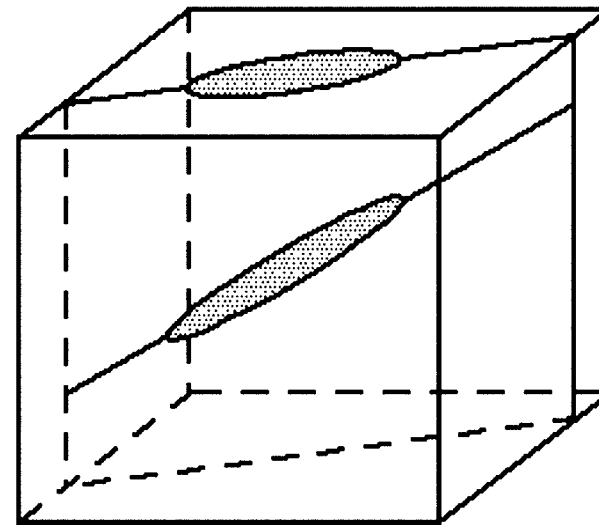

FIGURE 12. Schematic representation of the identification of the lineation through the migmatitic garnet-amphibolite. The oval on the top of the cube represents the long dimension of the leucosomes in the top scan in the stack of HR X-ray CT scans of the migmatitic garnet-amphibolite sample. The vertical slice directly beneath that represents a reslice of the stack, similar to the reslicing in Figure 11. The oval in the reslice represents the long dimension of the leucosome. This is the lineation defined by leucosome in the sample.

In the stromatic migmatite, the spatial relationship of the garnet crystals to the leucosome boundaries is made clear in a projection of a three-dimensional image (Fig. 16) by rendering the low-density material (leucosome) transparent and emphasizing with brighter color the high-density material (garnet). Garnet grains in the leucosomes are only locally in contact with the melanosome or mesosome (Fig. 16); apparently they are never in contact with melanosome or mesosome on both sides of the leucosome. Jones and Brown (1990) suggested that one reaction responsible for the production of melt was Bt + Als + Qtz (+ Pl) = Grt ± Kfs + L. The garnet observed in the leucosomes is likely to be the product of this moderate-to-low a_{H2O}, incongruent, biotite-dehydration melt-producing reaction, which suggests that its present geometry represents suspension in melt. Although this might have affected the viscosity of the melt, it did not affect the tortuosity of the channel through which the melt/magma flowed. If the leucosome walls had impinged on the garnet, in-plane tortuosity would have increased, as melt would have had to flow around the pinned garnet grains (Cook et al. 1990). Since the permeability structure is largely planar, the effect of pinned garnets in the channels will be minor unless the volumetric proportion of crystals is high. In contrast, pinned crystals of tabular feldspar, whether residual, peritectic, or cumulate, potentially will increase in-plane tortuosity and inhibit expulsion of residual melt during the waning stages of flow and lock-up.

It could be argued that the planarity of the leucosomes is not a primary feature of the melt-flow conduits but a secondary feature due to subsolidus deformation. This is unlikely to be the case because the microstructure of the leucosomes is

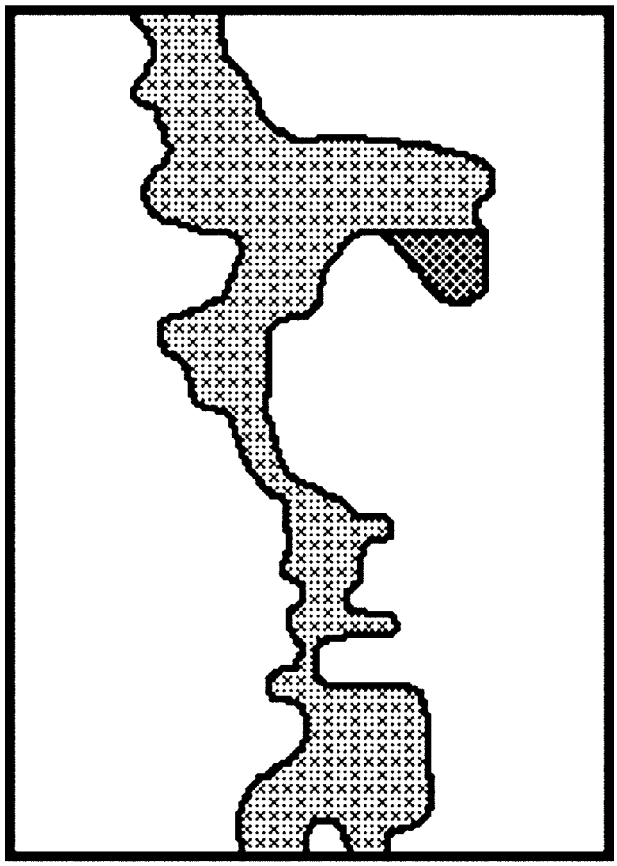

FIGURE 13. Schematic two-dimensional representation of leucosome connectivity perpendicular to plane of scans. Connectivity is first determined working from the top slice to the bottom by leucosome overlap from slice to slice. After this step all of the shaded area is selected; however, it includes a dead end in dark gray. When the process is repeated from the bottom slice to the top, the dead end is not included.

TABLE 1. Tortuosity of twenty measured paths through a connectivity tree in the migmatitic garnet-amphibolite sample

	Tortuosity	Minimum cross-sectional area (mm^2)	Maximum cross-sectional area (mm^2)	Average cross-sectional area (mm^2)
	2.22	0.4	103.0	36.2
	3.55	0.7	178.6	43.3
	2.59	0.4	151.3	30.9
	4.63	0.3	236.9	51.6
	2.82	0.5	151.3	26.6
	4.30	0.3	236.9	56.9
	4.65	0.3	236.9	48.2
	2.49	0.5	151.3	26.9
	2.67	4.3	151.3	40.0
	4.23	0.3	236.9	57.5
	5.85	0.9	262.1	65.0
	3.01	0.2	89.0	42.3
	3.63	0.1	125.8	39.2
	3.53	0.4	182.0	44.1
	3.65	0.3	130.4	32.7
	2.89	0.4	89.0	29.4
	4.07	1.0	140.8	42.4
	2.26	1.8	175.5	38.7
	2.82	0.6	114.3	36.4
	5.54	4.8	262.1	68.8
Avg	3.57	0.9	170.3	42.8

largely magmatic, with some plagioclase crystals that have euhedral faces against quartz and some quartz that occurs as grain boundary films between plagioclase crystals; quartz shows only slight undulose extinction. Based on these observations, we infer that any post-crystalline deformation has not modified the leucosome structure.

In the migmatitic garnet-amphibolite, leucosome is next to garnet in strain shadows (Williams et al. 1995). The spindle-shaped pockets of leucosome define a linear fabric (Figs. 5c and 17). In sections cut approximately perpendicular to the lineation, garnet crystals cut close to the center plane are in direct contact with the surrounding melanosome, with no leucosome next to the crystal faces unless that leucosome is associated with another garnet grain (Fig. 5c). This pattern of spindle-shaped pockets of leucosome is consistent with constrictional strain. If we consider the leucosome in these strain shadows to represent former melt, the garnet crystals in the current geometry represent obstacles to flow along a linear path. Even if the porosity of the active melt-flow network was higher than we infer from the leucosome volume, blocking of the channels by garnet would have contributed to the high degree of tortuosity of melt-flow paths through this sample.

Although the details of partial melting in amphibolite protoliths and the formation of melt lenses are beyond the scope of the present paper, leucosomes in the migmatitic garnet-amphibolite may have formed by a mechanism similar to that described in quartzo-feldspathic gneiss by Hand and Dirks (1992). In this model, melt-producing reactions occur initially in regions of higher strain where the melting reaction activation energy was first overstepped. Once nucleation of reaction products has occurred, these zones become the sites for continued melting to result in the formation of leucosomes with a higher melt component than the remainder of the rock. Hand and Dirks (1992) argue that in a differential stress field, diffusional processes will cause elongation of the leucosomes parallel to σ_1, ultimately to create an interconnected melt flow network.

The microstructural evidence for strain in the leucosomes suggests that deformation continued into the subsolidus, which may be interpreted to mean that the leucosome geometry had been altered from the geometry of the melt flow network, although we cannot determine if the deformation was sufficient to accomplish such a modification. Constrictional strain while melt was present (or after crystallization) may have caused pinching off to isolate pods of melt, now represented by leucosome, which would decrease connectivity and effective porosity for flow. For peridotite, Daines and Kohlstedt (1997) have shown that hydrostatic annealing of deformed samples results in a redistribution of melt into pockets oriented closer to perpendicular to the original syn-melting σ_1 than the original orientation of these melt pockets formed under an applied differential stress. Whether there is any redistribution of melt due to hydrostatic annealing in crustal protoliths is unknown.

Melt-flow networks are controlled in part by the tectonite fabric and the mineralogy of the rock, as illustrated by the samples in this study. When a schistose pelitic rock begins to melt, for example the protolith of the stromatic migmatite in this study, which has an S > L tectonite fabric reflecting apparent flattening strain, channeling of melt is constrained by the

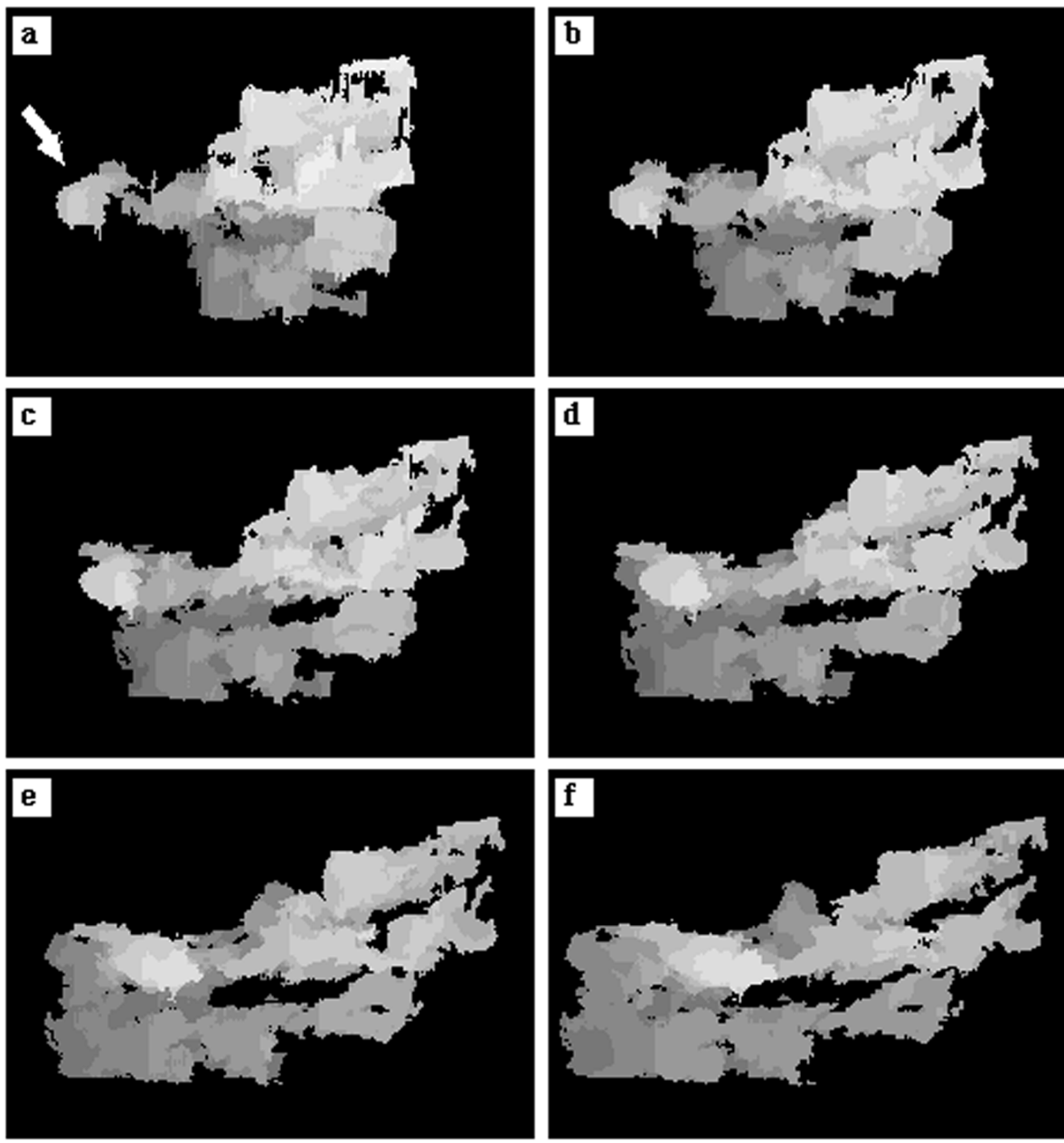

FIGURE 14. Projections of three-dimensional image of a single connectivity tree in the migmatitic garnet-amphibolite. The stack was rotated around a virtual vertical axis in the plane of the page through 50° at 10° intervals to produce views **a**–**f**. (Note that this axis of rotation is different from the axis in Figs. 7–10). A scale bar is not presented because these are projections of a three-dimensional image (Fig. 5a contains the scale for the first image in the stack). The arrow points to the leucosome in the top scan of the stack. This leucosome rotates toward the viewer from (**a**) to (**f**) so that in (**f**) the viewer is almost looking directly down on the stack. Note that a complex tree of leucosomes throughout the stack is connected to a single leucosome on the top of the stack. (**g**) Animated gif of projection of three-dimensional image rotating through 360°, at URLs http://www.minsocam.org and http://www.geol.umd.edu/~maryanne/AM/manuscript.html.

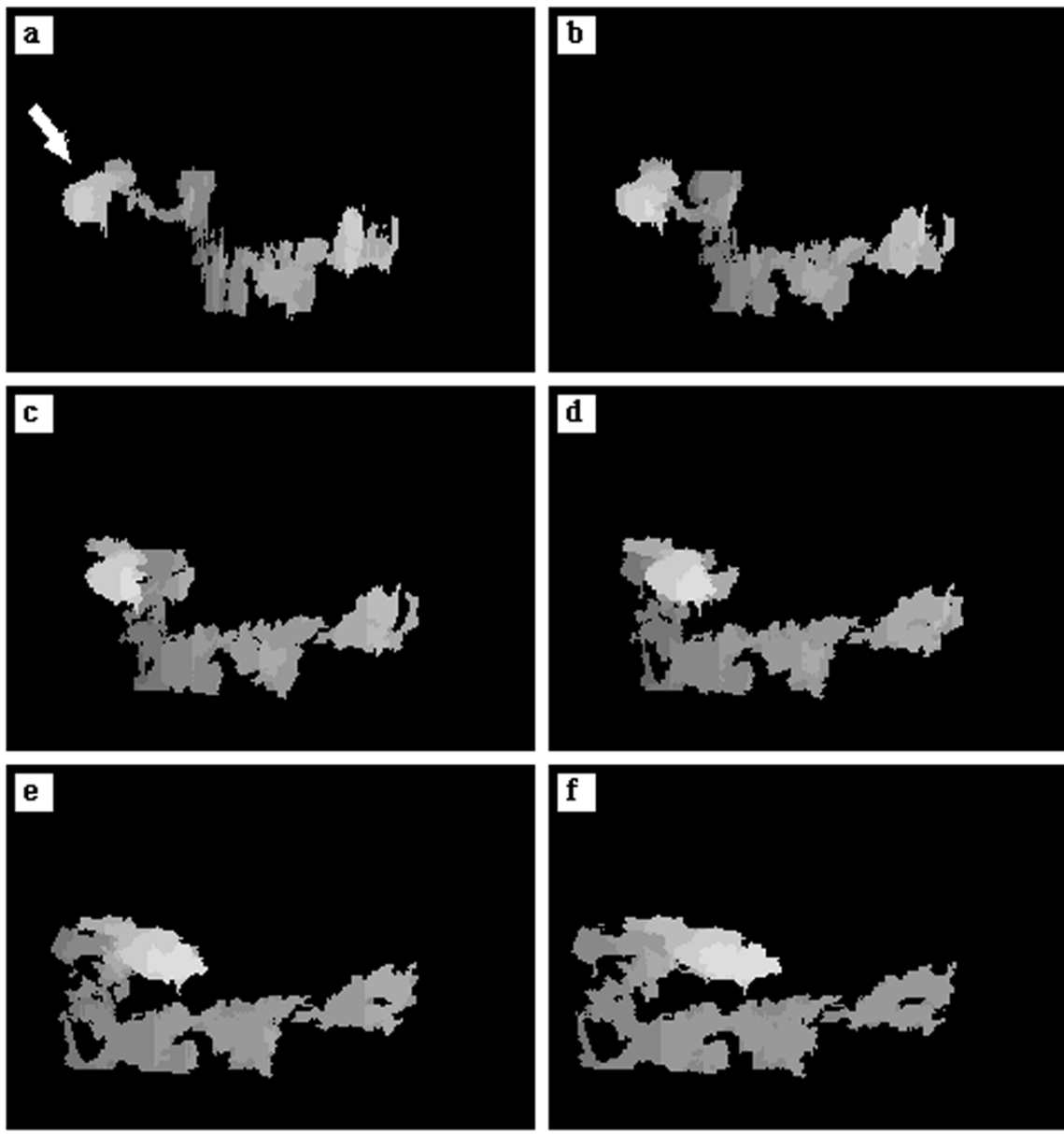

FIGURE 15. Projections of three-dimensional image of a single path within the connectivity tree in Figure 14. The stack was rotated around a virtual vertical axis in the plane of the page through 50° at 10° intervals to produce views **a**–**f**. (Note that this axis of rotation is different from the axis in Figs. 7–10.) The arrow points to the same leucosome in the top scan of the stack depicted in Figure 14. Note that the path includes a few very narrow necks through which fluid must flow. (**g**) Animated gif of projection of three-dimensional image rotating through 360°, located at URLs http://www.minsocam.org and http://www.geol.umd.edu/~maryanne/AM/manuscript.html.

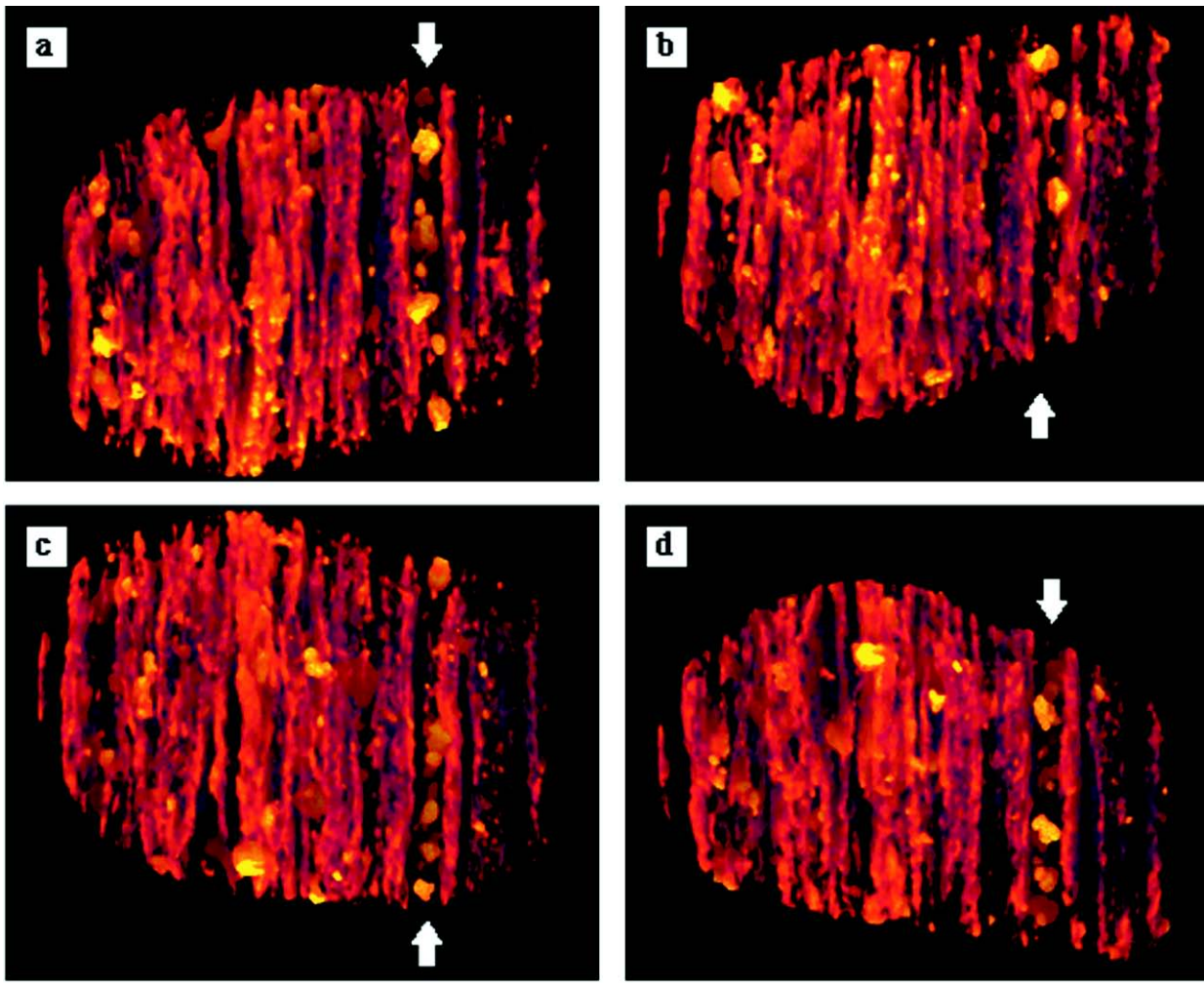

FIGURE 16. Projections of false-color, three-dimensional image of stromatic migmatite. The stack was rotated around a virtual horizontal axis in the plane of the page through 40, 120, 220, and 290° to produce views **a**–**d**, respectively. A scale bar is not presented because these are projections of a three-dimensional image (Fig. 4b contains the scale for the first image in the stack). The leucosome is rendered transparent in this image. The color of the solid part of the image is brighter for material with higher mineral density, with garnet appearing yellow. The arrow shows a leucosome in which many garnet crystals are "suspended". (**e**) Animation of projection of false-color three-dimensional image of stromatic migmatite, derived from the stack of two-dimensional representations of the HR X-ray CT scans, created using VoxBlast, and located at URLs http://www.minsocam.org and http://www.geol.umd.edu/~maryanne/AM/manuscript.html.

existing fabric, which is defined largely by the preferred orientation of the micaceous minerals, and the continuing contemporaneous deformation that progressively modifies the fabric, leading to the development of a stromatic structure. This tectonite fabric developed in response to deformation and/or transposition of original sedimentary layering, and deformation generally enhances the development of planar melt channels (e.g., Stevenson 1989; Hand and Dirks 1992; Maaløe 1992; Brown et al. 1995b; Tanner and Behrmann 1997).

When amphibolites with L > S tectonite fabrics, reflecting apparent constrictional strain, begin to melt, the melt channels are more linear than planar, as confirmed by our results. We infer that melt was channeled along the linear fabric, which is implied by the geometry of the leucosome in three-dimensions (Fig. 17). The high tortuosity of the migmatitic garnet-amphibolite may be taken to suggest that melt migrates out of partially molten amphibolite more slowly than out of partially molten pelite with planar melt channels. If correct, such a difference in flow rate may cause buildup of melt pressure and melt-enhanced embrittlement that leads to rock fracture. This may be reflected in the common development of agmatite structure in amphibolite protoliths. However, such an interpretation is not necessarily correct.

Using the theoretical k-ϕ relationships presented in Appendix 1 for network models of permeability based on tubular and crack porosity structures (Eqs. A3 and A7, respectively), it is apparent that permeability is strongly dependent on the radius of the tubes or the aperture of the cracks. Thus, for similar porosity, either the tubular network or the crack network could have larger k, depending on the radius/aperture values. For equal

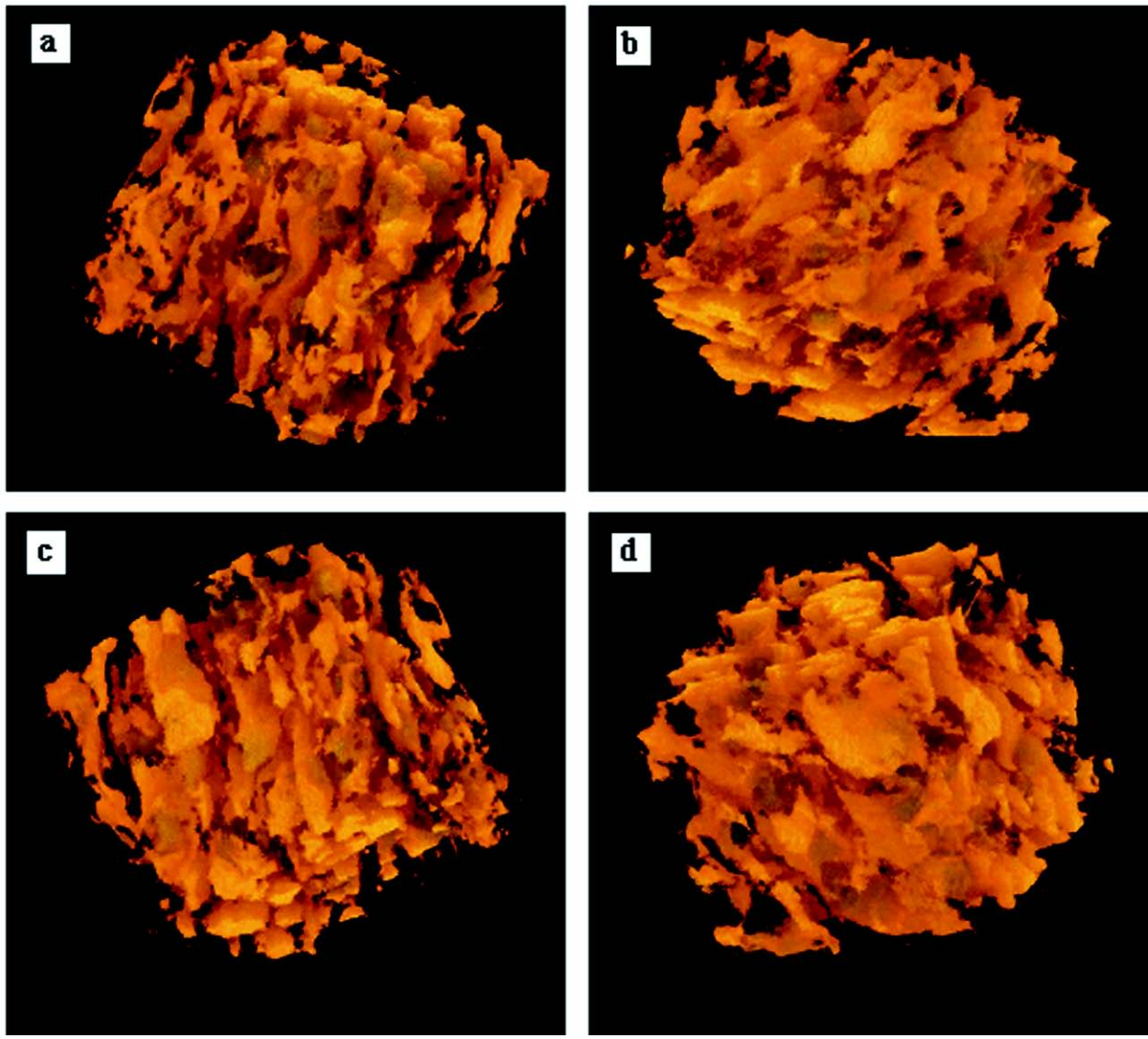

FIGURE 17. Projections of false-color three-dimensional image of leucosome geometry in migmatitic garnet-amphibolite (only the central part of the scanned volume is shown, cf., Figs. 6 and 10). The stack was rotated around a virtual vertical axis in the plane of the page through 90, 190, and 275° to produce views **b**–**d**, with respect to view (**a**). A scale bar is not presented because these are projections of a three-dimensional image (Fig. 5b contains the scale for the first image in the stack). Garnet associated with the leucosome and the matrix have been rendered transparent in this image. (**e**) Animation of projection of false-color three-dimensional image of leucosome in the migmatitic garnet-amphibolite, derived from the two-dimensional representations of the HR X-ray CT scans, created using VoxBlast, and at URLs http://www.minsocam.org and http://www.geol.umd.edu/~maryanne/AM/manuscript.html.

porosity, an ideal tubular network will have a permeability that is 33% greater than an ideal crack network, if the tube radius in the tubular network is equal to the crack aperture in the crack network. On the other hand, the crack network will have a 66% greater k than the tubular network if the tube radius in the tubular network is half the fracture aperture in the fracture network. Thus, for the same amount of melt (or porosity), there is no a priori requirement that k in L > S rocks be less than k in S > L rocks. The relative values of k for natural networks depend more strongly on the size of the conduits, than on their shape, at least for the idealized networks represented by Equations A3 and A7. For more complex networks, with more contorted flow paths, tortuosity will be an important factor in determining permeability. Whereas in this study the migmatitic garnet-amphibolite has more tortuous melt flow pathways than the stromatic migmatite, we do not imply that this is necessarily always the case. Other L > S migmatites may show greater lineation-parallel extent of conduits, or fewer obstacles like mineral grains than does the migmatitic garnet-amphibolite used in this study. Because of this, the reader should not draw the general conclusion that L > S rocks are expected to have lower k than S > L rocks.

We have shown that tortuosity is an important aspect of the geometry of the melt-flow network that affects melt-flow rate through the anatectic zone. An important part of the total effect of tortuosity on flow rate stems from the loss of energy due to the angular difference between the local streamline and the pressure gradient (Clennell 1997). Thus, any comparison of specific flow rates must account for obliquity between the pressure gradient and the melt-flow path through the melt-flow network. A similar effect might be expected at the crustal scale if the anisotropy of permeability of the melt flow network in the anatectic zone is not parallel to the larger-scale pressure gradient, which is likely to be dominated by buoyancy forces and reflect the magmastatic head (e.g., Brown and Solar 1998a). Finally, we have ignored the question of variations in viscosity, both between melts derived from different protolith compositions and due to variations in crystal content and/or water content. Viscosity is an important factor that must be incorporated when specific flow rates are determined and compared.

The introduction of microtomography (Flannery et al. 1987) has allowed three-dimensional numerical simulation of fluid flow through sandstones (Spanne et al. 1994; Auzerais et al. 1996; van Genabeek and Rothman 1996). These simulations have been successful, in that resulting model permeabilities match measured permeability (Spanne et al. 1994; Auzerais et al. 1996). Though quantitative measures of tortuosity are useful in comparing geometries of melt-flow networks, numerical simulations of melt flow through the three-dimensional porosity structure of migmatites, as represented by their leucosome geometry, are likely to provide a more accurate and detailed understanding of melt extraction rates from the anatectic zone, and this is the next goal of our research.

ACKNOWLEDGMENTS

M.A.B. and M.B. acknowledge discussions with and help from Phil Candela and Phil Piccoli. M.A.B. was supported by National Science Foundation and University of Maryland Graduate Fellowships, with additional support from the Department of Geology, University of Maryland. The HR X-ray CT facility at the University of Texas was made possible by grant support from the W.M. Keck Foundation, the National Science Foundation, and the Geology Foundation of University of Texas at Austin. The HR X-ray CT work was supported by the National Science Foundation through award EAR 9417764 (to W.D.C.). The University of Maryland, College Park and the Geology Foundation of the University of Texas at Austin defrayed the costs of publication. We thank Scott Johnson, Nathalie Marchildon, Tracy Rushmer, and Ron Vernon for helpful reviews and editorial comment, and Jeanne Martin for skilled word processing support.

REFERENCES CITED

Aharonov, E., Rothman, D.H., and Thompson, A.H. (1997) Transport properties and diagenesis in sedimentary rocks: The role of micro-scale geometry. Geology, 25, 547–550.

Amyx, J.W., Bass Jr., D.M., and Whitting, R.L. (1960) Petroleum Reservoir Engineering, Physical Properties, 610 p. McGraw-Hill, New York.

Ashworth, J.R. (1985) Migmatites, 302 p. Blackie, Glasgow.

Ashworth, J.R. and Brown, M. (1990) High-temperature Metamorphism and Crustal Anatexis. The Mineralogical Society Series, 2, 407 p. Unwin Hyman, London.

Auzerais, F.M., Dunsmuir, J., Ferréol, B.B., Martys, N., Olson, J., Ramakrishnan, T.S., Rothman, D.H., and Schwartz, L.M. (1996) Transport in sandstone: A study based on three dimensional microtomography. Geophysical Research Letters, 23, 705–708.

Bagdassarov, N. and Dorfman, A. (1998) Granite rheology: Magma flow and melt migration. Journal of the Geological Society, London, 155, 863–872.

Baker, D.R. (1996) Granitic melt viscosities: Empirical and configurational entropy models for their calculation. American Mineralogist, 81, 126–134.

Barboza, S.A. and Bergantz, G.W. (1998) Rheological transitions and the progress of melting in crustal rocks. Earth and Planetary Science Letters, 158, 19–29.

Bauer, R.L., Ketcham, R.A., Denison, C., and Carlson, W.D. (1998) X-ray computed tomography (CT) imaging of spiral inclusion trails and the external morphology of garnet porphyroblasts. Eos, Transactions, American Geophysical Union, 79, Supplement, April 28, 1998, S357.

Bear, J. (1972) Dynamics of Fluids in Porous Media, 764 p. American Elsevier, New York.

Bernabé, Y. (1991) Pore geometry and pressure dependence of the transport properties in sandstones. Geophysics, 56, 436–446.

——(1995) The transport properties of networks of cracks and pores. Journal of Geophysical Research, 100, 4231–4241.

Bernabé, Y. and Bruderer, C. (1998) Effect of the variance of pore size distribution on the transport properties of heterogeneous networks. Journal of Geophysical Research, 103, 513–525.

Blumenfeld, P. and Bouchez, J.L. (1988) Shear criteria in granite and migmatite deformed in the magmatic and solid states. Journal of Structural Geology, 10, 361–372.

Bouchez, J.L., Hutton, D.H.W., and Stephens, W.E. (1997) Granite: From Segregation of Melt to Emplacement Fabrics, 358 p. Kluwer Academic Publishers, The Netherlands.

Brown, M. (1983) The petrogenesis of some migmatites from the Presqu'ile de Rhuys, southern Brittany, France. In M.P. Atherton and C.D. Gribble, Eds., Migmatites, Melting and Metamorphism, 174–200. Shiva Publishing Limited, Nantwich.

——(1994) The generation, segregation, ascent and emplacement of granite magma: The migmatite-to-crustally-derived granite connection in thickened orogens. Earth-Science Reviews, 36, 83–130.

——(1998) Unpairing metamorphic belts: *P-T* paths and a tectonic model for the Ryoke Belt, southwest Japan. Journal of Metamorphic Geology, 16, 3–22.

Brown, M. and Dallmeyer, R.D. (1996) Rapid Variscan exhumation and role of magma in core complex formation: Southern Brittany metamorphic belt, France. Journal of Metamorphic Geology, 14, 361–379.

Brown, M. and Rushmer, T. (1997) The role of deformation in the movement of granitic melt: Views from the laboratory and the field. In M.B. Holness, Ed., Deformation-Enhanced Fluid Transport in the Earth's Crust and Mantle, p. 111–144. The Mineralogical Society Series, 8. Chapman and Hall, London.

Brown, M. and Solar, G.S. (1998a) Shear-zone systems and melts: feedback relations and self-organization in orogenic belts. Journal of Structural Geology, 20, 211–227.

——(1998b) Granite ascent and emplacement during contractional deformation in convergent orogens. Journal of Structural Geology, 20, 1365–1393

——(1999) Observations on the mechanism of syntectonic ascent and emplacement of granite magma in an obliquely convergent (transpressive) orogen. Tectonophysics, in press.

Brown, M., Rushmer, T., and Sawyer, E.W. (1995a) Special section: Mechanisms and consequences of melt segregation from crustal protoliths. Journal of Geophysical Research, 100, 15,549–15,805.

Brown, M., Averkin, Y., McLellan, E., and Sawyer, E. (1995b) Melt segregation in migmatites. Journal of Geophysical Research, 100, 15,655–15,679.

Brown, M., Candela, P.A., Peck, D., Stephens, W.E., Walker, R.J., and Zen, E. (1996) Origin of Granites and Related Rocks, 361 p. Geological Society, of America Special Paper, 315.

Brown, P.E. and Chappell, B.W. (1992) Second Hutton symposium: The origin of granites and related rocks. Transactions, Royal Society of Edinburgh: Earth Sciences, 83, 1–506.

Bryon, D.N., Atherton, M.P., and Hunter, R.H. (1995) The interpretation of granitic textures from serial thin sectioning, image analysis and three-dimensional reconstruction. Mineralogical Magazine, 58, 201–211.

Bryon, D.N., Atherton, M.P., Cheadle, M.J., and Hunter, R.H. (1996) Melt movement and the occlusion of porosity in crystallizing granitic systems. Mineralogical Magazine, 60, 163–171.

Büsch, W., Schneider, G., and Mehnert, K.R. (1974) Initial melting at grain boundaries. Part II: Melting in rocks of granodioritic, quartz dioritic and tonalitic composition. Neues Jahrbuch fur Mineralogie, Monatshefte, 8, 345–370.

Carlson, W.D. and Denison, C. (1992) Mechanisms of porphyroblast crystallization: Results from high-resolution computed X-ray tomography. Science, 257, 1,236–1,239.

Carman, P.C. (1937) Fluid flow through granular beds. Transactions of the Institution of Chemical Engineers, 15, 150–166.

Carson, C.J., Powell, R., Wilson, C.J.L., and Dirks, P.H.H.M. (1997) Partial melting during tectonic exhumation of a granulite terrane: an example from the Larsemann Hills, East Antarctica. Journal of Metamorphic Geology, 15, 105–126.

Clemens, J.D., Petford, N., and Mawer, C.K. (1997) Ascent mechanisms of granitic magmas: Causes and consequences. In M.B. Holness, Ed., Deformation-Enhanced Fluid Transport in the Earth's Crust and Mantle, 28 p. The Mineralogical Society Series, 8, Chapman and Hall, London.

Clennell, M.B. (1997) Tortuosity: A guide through the maze. In M.A. Lovell and P.K. Harvey, Eds., Developments in Petrophysics, 299–344. Geological Society, London, Special Publications, 122, London.

Collins, W.J. and Sawyer, E.W. (1996) Pervasive magma transfer through the lower-middle crust during non-coaxial compressional deformation: An alternative to

diking. Journal of Metamorphic Geology, 14, 565–579.
Connolly, J.A.D. and Podladchikov, Yu.Yu. (1998) Compaction-driven fluid flow in viscoelastic rock. Geodinamica Acta, 11, 55–84.
Cook, A.M., Myer, L.R., Cook, N.G.W., and Doyle, F.M. (1990) The effects of tortuosity on flow through a natural fracture. In W.A. Hastrulid and G.A. Johnson, Eds., Rock Mechanics Contributions and Challenges: Proceedings of the 31st U.S. Symposium, p. 371–378. Balkema, Rotterdam.
Cooper, M.R. and Hunter, H.R. (1995) Precision serial-lapping imaging and three-dimensional reconstruction of minus-cement and post-cementation intergranular pore-systems in the Penrith Sandstone of north-western England. Mineralogical Magazine, 59, 213–220.
Daines, M.J. and Kohlstedt, D.L. (1997) Influence of deformation on melt topology in peridotites. Journal of Geophysical Research, 102, 10,257–10,271.
Dallain, C., Schulmann, K., and Ledru, P. (1999) Textural evolution in the transition from subsolidus annealing to melting process, Velay Dome, French Massif Central. Journal of Metamorphic Geology, 17, 61–74.
Daniel, C.G. and Spear, F.S. (1998) Three-dimensional patterns of garnet nucleation and growth. Geology, 26, 503–506.
David, C. (1993) Geometry of flow paths for fluid transport in rocks. Journal of Geophysical Research, 87, 12,267–12,278.
David, C., Guéguen, Y., and Pampoukis, G. (1990) Effective medium theory and network theory applied to transport properties of rocks. Journal of Geophysical Research, 95, 6993–7005.
Davidson, C., Schmid, S.M., Hollister, L.S. (1994) Role of melt during deformation in the deep crust. TERRA Nova 6, 133–142.
Denison, C. and Carlson, W.D. (1997) Three-dimensional quantitative textural analysis of metamorphic rocks using high-resolution computed X-ray tomography: Part II. Application to natural samples. Journal of Metamorphic Geology, 15, 45–57.
Denison, C., Carlson, W.D., and Ketcham, R.A. (1997) Three-dimensional quantitative textural analysis of metamorphic rocks using high-resolution computed X-ray tomography: Part I. Methods and techniques. Journal of Metamorphic Geology, 15, 29–44.
Diedericks, G.P.J. and Du Plessis, J.P. (1995) On tortuosity and areosity tensors for porous media. Transport in Porous Media, 20, 265–279.
Dougan, T.W. (1979) Compositional and modal relationships and melting relationships in some migmatitic metapelites from New Hampshire and Maine. American Journal of Science, 279, 897–935.
——(1981) Melting reactions and trace element relationships in selected specimens of migmatitic pelites from New Hampshire and Maine. Contributions to Mineralogy and Petrology, 78, 337–344.
Doyle, W. (1962) Operations useful of similarity-invariant pattern recognition. Journal of the Association for Computing Machinery, 9, 259–267.
Ellis, D.J. and Obata, M. (1992) Migmatite and melt segregation at Cooma, New South Wales. Transactions of the Royal Society of Edinburgh, Earth Sciences, 83, 95–106.
Feng, C. and Stewart, W.E. (1973) Practical models for isothermal diffusion and flow of gases in porous solids. Industrial and Engineering Chemistry Fundamentals, 12, 143–147.
Flannery, B.P., Deckman, H.W., Roberge, W.G., and D'Amico, K.L. (1987) Three-dimensional X-ray microtomography. Science, 237, 1,439–1,444.
Guéguen, Y. and Dienes, J. (1989) Transport properties of rocks from statistics and percolation. Mathematical Geology, 21, 1–13.
Guéguen, Y. and Palciauskas V. (1994) Introduction to the physics of rocks, 294 p. Princeton University Press, Princeton, New Jersey.
Hand, M. and Dirks, P.H.G.M. (1992) The influence of deformation on the formation of axial-planar leucosomes and the segregation of small melt bodies within the migmatitic Napperby Gneiss, Central Australia. Journal of Structural Geology, 14, 591–604.
Harte, B., Pattison, D.R.M., and Linklater, C.M. (1991) Field relations and petrography of partially melted pelitic and semi-pelitic rocks. In G. Voll, J. Töpel, D.R.M. Pattison, and F Seifert, Eds., Equilibrium and kinetics in contact metamorphism: The Ballachulish igneous complex and its aureole, p. 81–210. Springer-Verlag, Berlin.
Hartel, T.H.D. and Pattison, D.R.M. (1996) Genesis of the Kapuskasing (Ontario) migmatitic mafic granulites by dehydration melting of amphibole: The importance of quartz to reaction progress.
Journal of Metamorphic Geology, 14, 591–611.
Holness, M. (1997) Deformation-Enhanced Fluid Transport in the Earth's Crust and Mantle, 333 p. The Mineralogical Society Series: 8. Chapman and Hall, London.
Hunter, R.H. (1987) Textural equilibrium in layered igneous rocks. In I. Parsons, Ed., Origins of igneous layering, 473–503. Reidel, Dortrecht, The Netherlands.
Johnson, D.L. and Sen, P.N. (1988) Dependence of the conductivity of a porous medium on electrolyte conductivity. Physics Reviews, B37, 3502–3510.
Johnson, S.E. (1993) Unraveling the spirals: A serial thin-section study and three-dimensional computer-aided reconstruction of spiral-shaped inclusion trains in garnet porphyroblasts. Journal of Metamorphic Geology, 11, 621–634.
Johnson, S.E. and Moore, R.R. (1996) De-bugging the "millipede" porphyroblast microstructure: A serial thin-section study and 3-D computer animation. Journal of Metamorphic Geology, 14, 3–13.
Jones, K.A. and Brown, M. (1990) High-temperature 'clockwise' P-T paths and melting int he development of regional migmatites: an example from southern Brittany, France. Journal of Metamorphic Geology, 8, 551–578.
Kostek, S., Schwartz, L.M., and Johnson, D.L. (1992) Fluid permeability in porous media: Comparisons of electrical estimates with hydrodynamical calculations. Physical Review, B45, 186–195.
Laporte, D. (1994) Wetting behavior of partial melts during crustal anatexis: the distribution of hydrous silicic melts in polycrystalline aggregates of quartz. Contributions to Mineralogy and Petrology, 116, 489–99.
Laporte, D. and Watson, E.B. (1995) Experimental and theoretical constraints on melt distribution in crustal sources: The effect of crystalline anisotropy on melt interconnectivity. Chemical Geology, 124, 161–184.
Laporte, D., Rapaille, C., and Provost, A. (1997) Wetting angles, equilibrium melt geometry, and the permeability threshold of partially molten crustal protoliths. In J.L. Bouchez, D. Hutton, and W.E. Stephens, Eds., Granite: From melt segregation to emplacement fabrics, 31–54. Kluwer Academic Publishers, Dordrecht, The Netherlands.
Lindquist, W.B., Lee, S.-M., Coker, D.A., Jones, K.W., and Spanne, P. (1996) Medial axis analysis of void structure in three-dimensional tomographic images of porous media. Journal of Geophysical Research, 101, 8297–8310.
Lupulescu, A. and Watson, E.B. (1999) Low melt fraction connectivity of granitic and tonalitic melts in a mafic crustal rock at 800 °C and 1 GPa. Contributions to Mineralogy and Petrology, 134, 202–216.
Maaløe, S. (1992) Melting and diffusion processes in closed-system migmatization. Journal of Metamorphic Geology, 10, 503–516.
Marschallinger, R. (1998a) Correction of geometric errors associated with the 3-D reconstruction of geological materials by precision serial lapping. Mineralogical Magazine, 62, 783–792.
——(1998b) Three-dimensional reconstruction and modeling of microstructures and microchemistry in geological materials. Scanning, 20, 65–73.
——(1998c) 3-D reconstruction and volume modelling of the grain fabric of geological materials. Physics and Chemistry of the Earth, 23, 267–271.
Marschallinger, R., Höck, V., and Topa, D. (1993) A method for the 3-D reconstruction of chemically zoned minerals from microprobe scanned serial sections. European Microscopy and Analysis, 26, 5–7.
McLellan, E.L. (1989) Sequential formation of sub-solidus and anatectic migmatites in response to thermal evolution, eastern Scotland. Journal of Geology, 97, 165–182.
Means, W.D. and Park, Y. (1994) New experimental approach to understanding igneous texture. Geology, 22, 323–326.
Mehnert, K.R., Büsch, W., and Schneider, G. (1973) Initial melting at grain boundaries of quartz and feldspar in gneisses and granulites. Neues Jahrbuch fur Mineralogie, Monatshefte, 4, 165–183.
Middleton, M.F. (1997) Measurements of streaming potential versus applied pressure for porous rocks. Physics and Chemistry of the Earth, 22, 81–86.
Miller, S.A. (1997) Ignoring permeability (k) in fluid-controlled crustal processes. Abstract supplement No. 1, TERRA Nova, 9, 646.
Nicolas, A. and Ildefonse, B. (1996) Flow mechanism and viscosity in basaltic magma chambers. Geophysical Research Letters, 23, 2013–2016.
Nyman, M.W., Pattison, D.R.M., and Ghent, E.D. (1995) Melt extraction during formation of K-feldspar + sillimanite migmatites, west of Revelstoke, British Columbia. Journal of Petrology, 36, 351–372.
Obata, M., Yoshimura, Y., Nagakawa, K., Odawara, S., and Osanai, Y. (1994) Crustal anatexis and melt migration in the Higo metamorphic terrane, west-central Kyushu, Kumamoto, Japan. Lithos, 32, 135–147.
O'Hara, K.D. (1994) Fluid-rock interaction in crustal shear zones: A directed percolation approach. Geology, 22, 843–846.
Ohashi, Y. (1992) Three-dimensional reconstruction of pore geometry from serial sections: Image algebraic approach. In R. Pflug and J.W. Harbaugh, Eds., Computer graphics in geology: Lecture Notes in Earth Sciences, 41, 63–76. Springer-Verlag, Berlin and Heidelberg.
Ord, A. and Henley, S. (1997) Fluid pumping: Some exploratory numerical models. Physics and Chemistry of the Earth, 22, 49–56.
Parney, R. and Smith, L. (1995) Fluid velocity and path length in fractured media. Geophysical Research Letters, 22, 1437–1440.
Paterson, S.R. and Miller, R.B. (1998) Mid-crustal magmatic sheets in the Cascades Mountains, Washington: Implications for magma ascent. Journal of Structural Geology, 20, 1345–1363.
Petford, N. and Koenders, M.A. (1998) Granular flow and viscous fluctuations in low Bagnold number granitic magmas. Journal of the Geological Society, London, 155, 873–881.
Petford, N., Paterson, B., McCaffrey, K., and Pugliese, S. (1996) Melt infiltration and advection in microdioritic enclaves. European Journal of Mineralogy, 8, 405–412.
Philpotts, A.R., Shi, J., and Brustman, C. (1998) Role of plagioclase crystal chains in the differentiation of partly crystallized basaltic magma. Nature, 395, 343–346.
Powell, R. and Downes, J. (1990) Garnet porphyroblast-bearing leucosomes in metapelites: Mechanisms, phase diagrams, and an example from Broken Hill,

Australia, In J.R. Ashworth and M. Brown, Eds., High-temperature metamorphism and crustal anatexis, p. 05–123. The Mineralogical Society Series, 2. Unwin Hyman, London.
Proussevitch, A., Ketcham, R., Carlson, W., and Sahagian, D. (1998) Preliminary results of X-ray CT analysis of Hawaiian vesicular basalts. Eos, Transactions, American Geophysical Union, 79, Supplement, April 28, 1998, S360.
Pugliese, S. and Petford, N. (1997) Pore structure visualization in microdioritic enclaves. In M.A. Lovellma and P.K. Harvey., Eds., Developments in petrophysics. Geological Society, London, Special Publications, 122, London.
Rushmer, T. (1999) Volume change during partial melting: Implications for melt extraction, melt geochemistry and crustal rheology. Tectonophysics, in press.
Ruth, D. and Suman, R. (1992) The role of microscopic cross flow in idealized porous media. Transport in Porous Media, 7, 103–125.
Rutter, E.H. (1997) The influence of deformation on the extraction of crustal melts: A consideration of the role of melt-assisted granular flow. In M. Holness, Ed., Deformation-Enhanced Fluid Transport in the Earth's Crust and Mantle, p. 82–110. The Mineralogical Society Series 8. Chapman and Hall, London.
Sahoo, P.K., Soltani, S., and Wong, A.K.C. (1988) A survey of thresholding techniques. Computer Vision, Graphics, and Image Processing, 41, 233–260.
Sawyer, E.W. (1994) Melt segregation in the continental crust. Geology , 22, 1019–1022.
——(1996) Melt-segregation and magma flow in migmatites: Implications for the generation of granite magmas. Transactions of the Royal Society of Edinburgh: Earth Sciences, 87, 85–94.
——(1998) Formation and evolution of granite magmas during crustal reworking: the significance of diatexites. Journal of Petrology, 39, 1147–1167.
——(1999) Criteria for the recognition of partial melting. Physics and Chemistry of the Earth, 00, 000–000.
Sawyer, E.W. and Barnes, S.-J. (1988) Temporal and compositional differences between subsolidus and anatectic migmatite leucosomes from the Quetico metasedimentary belt, Canada. Journal of Metamorphic Geology, 6, 437–450.
Scaillet, B., Holtz, F., and Pichavant, M. (1997) Rheological properties of granitic magmas in their crystallization range. In J.L. Bouchez, D. Hutton, and W.E. Stephens, Eds., Granite: From melt segregation to emplacement fabrics, p. 11–29. Kluwer Academic Publishers, Dordrecht, The Netherlands.
Schnetger, B. (1994) Partial melting during the evolution of the amphibolite-to-granulite-facies gneisses of the Ivrea Zone, northern Italy. Chemical Geology, 112, 71–101.
Schwartz, L.M., Sen, P.N., and Johnson, D.L. (1989) Influence of rough surfaces on electrolytic conduction in porous media. Physics Reviews, B40, 2450–2458.
Snoke, A.W., Kalakay, T.J., Quick, J.E., and Sinigoi, S. (1999) Deep-crustal shear zone as a result of mafic igneous intrusion in the lower crust, Ivrea-Verbano Zone, Southern Alps, Italy. Earth and Planetary Science Letters, 166, 31–45.
Spanne, P., Thovert, J.F., Jacquin, C.J., Lindquist, W.B., Jones, K.W., and Adler, P.M. (1994) Synchrotron computed microtomography of porous media: Topology and transports. Physical Review Letters, 73, 2001–2004.
Spear, F.S., Kohn, M.J., and Cheney, J.T. (1999) P-T paths from anatectic pelites. Contributions to Mineralogy and Petrology, 134, 17–32.
Stauffer, D. and Aharony, A. (1994) Introduction to percolation theory. Taylor and Francis, London.
Stevenson, D.J. (1989) Spontaneous small-scale melt segregation in partial melts undergoing deformation. Geophysical Research Letters, 16, 1067–1070.
Suman R. and Ruth, D. (1993) Formation factor and tortuosity of homogeneous porous media. Transport in Porous Media, 12, 185–206.
Tanner, D.C. (1999) The scale-invariant nature of migmatite from the Oberpfalz, NE Bavaria and its significance for melt transport. Tectonophysics, 302, 297–305.
Tanner, D.C. and Behrmann, J.H. (1997) Study of strain and partial-melt transfer in a banded migmatite. Journal of Structural Geology, 19, 1405–1417.
Thompson, A., Katz, A., and Krohn, C. (1987) The microgeometry and transport properties of sedimentary rocks. Advances in Physics, 36, 625–694.
van Genabeek, O. and Rothman, D.H. (1996) Macroscopic manifestations of microscopic flows through porous media: Phenomenology from simulation. Annual Reviews in Earth and Planetary Sciences, 24, 63–87.
Vernon, R.H. (1999) Quartz and feldspar microstructures in metamorphic rocks. Canadian Mineralogist, 37, 513–524.
Vernon, R.H. and Collins, W.J. (1988) Igneous microstructures in migmatites. Geology, 16, 1126–1129.
Vernon, R.H. and Paterson, S.R. (1999) Axial-surface leucosomes in anatectic migmatites. Tectonophysics, in press.
Vielzeuf, D. and Vidal, P. (1990) Granulites and crustal evolution, 585 p. Kluwer Academic Publishers, Norwell, The Netherlands.
Vigneresse, J.-L., Barbey, P., and Cuney, M. (1997) Rheological transitions during partial melting and crystallization with application to felsic magma segregation and transfer. Journal of Petrology, 70, 1579–1600.
Von Bargen, N. and Waff, H.S. (1986) Permeabilities, interfacial areas and curvatures of partially molten systems: Results of numerical computations of equilibrium microstructures. Journal of Geophysical Research, 91, 9261–9276.
Walsh, J.B. and Brace, W.F. (1984) The effect of pressure on porosity and the transport properties of rock. Journal of Geophysical Research, 89, 9425–9431.
Weber, C., Barbey, P., Cuney, M., and Martin, H. (1985) Trace element behavior during migmatization. Evidence for a complex melt-residuum-fluid interaction in the St. Malo migmatitic dome (France). Contributions to Mineralogy and Petrology, 90, 52–62.
Williams, M.L., Hanmer, S., Kopf, C., and Darrach, M. (1995) Syntectonic generation and segregation of tonalitic melts from amphibolite dikes in the lower crust, Striding-Athabasca mylonite zone, northern Saskatchewan. Journal of Geophysical Research, 100, 15,717–15,734.
Wolf, M.B. and Wyllie, P.J. (1991) Dehydration-melting of solid amphibolite at 10 kbar. Textural development, liquid interconnectivity and applications to the segregation of magma. Mineralogy and Petrology, 44, 151–179.

MANUSCRIPT RECEIVED NOVEMBER 16, 1998
MANUSCRIPT ACCEPTED JUNE 11, 1999
PAPER HANDLED BY SCOTT E. JOHNSON

APPENDIX 1. PERMEABILITY MODELS

Network models

At the grain scale, the melt-flow network in partially molten crustal rocks is likely to consist of tubular pores with triangular cross-sections at three-grain junctions, sheet-like channels at two-grain interfaces, and roughly equidimensional pockets at four-grain junctions. Network models use three kinds of pore space, tubes, penny-shaped cracks, and spherical pores, connected to form simple physical analogs of rock pore structure (e.g., Bernabé 1991). These models can be used to form either continuous three-dimensional networks of porosity to examine how variations in pore geometry can affect transport properties, or to examine the effect of variations in the connectivity of pore space (David et al. 1990; Bernabé and Bruderer 1998).

Consider a model in which the pore volume is represented by a homogeneous and isotropic distribution of straight, parallel tubes of variable length, d, and variable radius, r. In the interior of a tube of radius r, fluid flows with an average pore velocity, $\bar{v}$, which is given by Poiseuille's law (Amyx et al. 1960)

$$\bar{v} = \frac{r^2}{8\mu}\frac{\mathrm{d}P}{\mathrm{d}x}. \quad \text{(A1)}$$

If the radii do not vary greatly, combining with the Dupuit-Forcheimer assumption ($q = \mathrm{v} \cdot \phi$) yields the volumetric flux, q, as follows

$$q = \frac{\bar{r}^2}{8\mu}\frac{\mathrm{d}P}{\mathrm{d}x}\phi, \quad \text{(A2)}$$

where $\bar{r}$ is mean radius. By comparison with Equation 1, we obtain

$$k = \frac{\bar{r}^2}{8}\phi. \quad \text{(A3)}$$

If the density of tubes is $N = (1/\bar{l}^3)$, where $\bar{l}$ is the average distance between tubes, then

$$\phi = \frac{\pi \bar{r}^2 \bar{d}}{\bar{l}^3}, \quad \text{(A4)}$$

which yields

$$\phi = \frac{\pi \bar{r}^2 \bar{d}}{\bar{l}^3}. \quad \text{(A5)}$$

Thus, the permeability is controlled by the distance between tubes, their lengths, and radii.

Similarly, we can calculate the permeability resulting from

a distribution of cracks of aperture 2*w* and diameter 2*c*. It can be shown (e.g., Guéguen and Palciauskas 1994) that

$$\bar{v} = \frac{\bar{w}^2}{3\mu}\frac{dP}{dx}, \quad q = \bar{v}\,\phi. \tag{A6}$$

By comparison with Equation 1, we obtain

$$k = \frac{\bar{w}^2}{3}\phi. \tag{A7}$$

For the same approximations discussed above,

$$\phi = 2\pi\frac{\bar{c}^2\,\bar{w}}{\bar{l}^3}, \tag{A8}$$

and

$$k = \frac{2\pi\bar{c}\,\bar{w}^3}{3\bar{l}^3}. \tag{A9}$$

Again, the permeability is controlled by the average distance between cracks, and the crack radii and apertures

Percolation

To determine permeability, it is necessary to understand the nature of the connected porosity; network models are used to examine the effect of varying connectivity on permeability using percolation theory (e.g., Stauffer and Aharony 1994). The tube and crack models discussed above assume a perfect connection among these microstructural features. Bernabé (1995) generated a large set of networks with variations in pore size and connectivity and found that $k \propto \phi^{2.44}$, which lies between the exponent of 3 for cracks and that of 2 for tubes (see above). Percolation theory evaluates the degree of network connectivity, so that the results of Equations A5 and A9 must be multiplied by a factor, *f*, that represents the fraction of tubes or cracks attached to the percolating cluster. Below the percolation threshold, connections are finite and model $k = 0$. Permeability increases rapidly above the percolation threshold and approaches the values given by Equations A5 and A9 (Guéguen and Palciauskas 1994). One strength of network models is the ease with which highly heterogeneous porous media can be simulated, and one outcome of this modeling is a better understanding of the control on permeability of a small fraction of the total connected pore space, emphasizing that variations in the bulk porosity may not be the only microstructural parameter that controls transport properties of rocks (Parney and Smith 1995). For melt flow in orogenic environments, we need to consider syn-anatectic deformation. Models for directed percolation are preferred to ordinary percolation models because directed percolation clusters have high length/width radios and anisotropic permeability that better simulate the natural environment in active orogenic belts (O'Hara 1994).

Equivalent porous-medium models

In the equivalent channel model, which is based on the assumption of a homogeneous material with no preferential flow paths and a completely connected pore space, the porous medium is presumed equivalent to a conduit with a highly complex cross-section of constant average area. The length scale governing the flow rate through the conduit is the hydraulic radius, which is the pore volume divided by the pore-surface area (or the flow cross-sectional area divided by the perimeter of the conduit). For a given porosity, as the size of the pores decreases, so their number must increase; therefore, the specific surface area increases as the inverse square of pore radius, which affects the drag force that a moving fluid exerts on the pore walls. Permeability in an equivalent channel model is described using the Kozeny-Carman equation

$$k = \frac{a\phi^3}{S^2(1-\phi)^2} \tag{A10}$$

where *a* is the Kozeny constant (<1), and *S* is the surface area of pores per unit volume of solids (Guéguen and Palciauskas 1994). The Kozeny-Carman model works well if the walls of the pores are smooth. Furthermore, the equivalent channel model can be made more realistic using an empirical weighting procedure to reduce the effects of dead-ends and other low-conductance pore space (e.g., Johnson and Sen 1988; Schwartz et al. 1989). Also, the Kozeny-Carman equation can be modified to take into account convoluted flow paths, using the idea of tortuosity, τ, discussed below. The main disadvantage of equivalent porous-medium models is the assumption that a single hydraulic radius represents the combined effects of the innumerable flow channels traversing the medium when the pore space in natural rocks is not homogeneous. Conduits in natural materials commonly vary widely in conductance, and equivalent channel models cannot predict transport properties accurately when the pore space involves a broad distribution of conductances (David et al. 1990; Bernabé and Bruderer 1998).

Tortuosity

Tortuosity, τ, has been defined in many ways in mathematical models of fluid flow through porous media (Carman 1937; Bear 1972; Diedericks and Du Plessis 1995; Clennell 1997). The conclusions of the mathematical models that the flux of fluid along a sinuous route will be lower than for a straight route, due to longer path length and loss of energy caused by the angular difference between the local streamline and the pressure gradient, are intuitive. The ratio of shortest flow path between inflow and outflow points, avoiding solid obstacles over the linear separation between these inflow and outflow points, is often called the geometrical tortuosity. This definition is not ideal because the geometrically shortest paths are not necessarily the least sinuous, which affects the efficiency of flow. This is evident from flow simulations in networks (e.g., Ruth and Suman 1992; Suman and Ruth 1993; David 1993; Bernabé 1995) and in representational flow models (e.g., Parney and Smith 1995). Carman (1937) prefers hydraulic tortuosity, which is the effective path length taken by the fluid, rather than the shortest possible path. Because of viscous drag, fluid flow is more retarded at the channel walls than along channel axes, so not all paths are equally favored. These issues are discussed at length in the reviews by Diedericks and Du Plessis (1995) and Clennell (1997). Besides definitions specific to a particular model of flow through porous media, the most useful basic definition of tortuosity is the path-length tortuosity, which is the ratio of the length of the flow path divided by the straight line length (L_e/L). Path-length tortuosity is most easily visual-

ized in a pore space consisting of single capillaries of constant width having no branching, in which case L_e corresponds to the line connecting midpoints in successive sections through the capillary. The Kozeny-Carman equation modified to take account of the tortuosity (Guéguen and Palciauskas 1994) becomes

$$k = \frac{1}{b\tau^2} \frac{\phi^3}{S^2(1-\phi)^2}, \quad \text{(A11)}$$

where the constant a has been replaced by a new constant that incorporates the effects of tortuosity $1/b\tau^2$, in which b is a constant. When the tortuosity becomes infinite, the fluid is no longer connected, which is equivalent to $f \rightarrow 0$ in percolation theory; thus, the notion of tortuosity and of percolation are directly related.

The lower limit of τ is 1, by definition. Carman (1937) determined by experiment a value of $\tau \sqrt{2}$ for flow through a medium of glass spheres, and theoretical calculation of τ based on a random pore structure in an unlithified sediment yields a value of $\tau = \sqrt{3}$ (Feng and Stewart 1973). Direct measurement of τ has only been undertaken since the development of microtomography. Measured τ of the Berea sandstone ranges from ~1.1 to 5.5 with a mode of ~2.0 (Lindquist et al. 1996). Flow paths in rocks are through pore spaces that have rough and convoluted walls, rather than cylindrical channels of uniform cross-section. The effect of these constrictions and bulges is to reduce the overall efficiency of the flow channels, as energy is expended accelerating and decelerating the melt, and in minor viscous losses as the streamlines diverge and converge. The effects of these local flow divergences have been discussed by Bernabé (1991).